



Epigenetic control of CD8+ T cell responsiveness to a-PD-1 by Suv39h1

Leticia Laura Niborski, Paul Gueguen, Mengliang Ye, Allan Thiolat, Rodrigo Nalio Ramos, Pamela Caudana, Jordan Denizeau, Christel Goudot, Jean-Michel Luccarini, Anne Soudé, et al.

► To cite this version:

Leticia Laura Niborski, Paul Gueguen, Mengliang Ye, Allan Thiolat, Rodrigo Nalio Ramos, et al.. Epigenetic control of CD8+ T cell responsiveness to a-PD-1 by Suv39h1: Contrôle épigénétique de la réactivité des cellules T CD8+ à l'a-PD-1 par Suv39h1. 2020. hal-03041343

HAL Id: hal-03041343

<https://hal.science/hal-03041343>

Preprint submitted on 4 Dec 2020

HAL is a multi-disciplinary open access archive for the deposit and dissemination of scientific research documents, whether they are published or not. The documents may come from teaching and research institutions in France or abroad, or from public or private research centers.

L'archive ouverte pluridisciplinaire **HAL**, est destinée au dépôt et à la diffusion de documents scientifiques de niveau recherche, publiés ou non, émanant des établissements d'enseignement et de recherche français ou étrangers, des laboratoires publics ou privés.

Copyright

Epigenetic control of CD8⁺ T cell responsiveness to anti-PD-1 by Suv39h1

Leticia Laura Niborski^{1,2,3}, Paul Gueguen^{1,2}, Mengliang Ye^{1,2}, Allan Thiolat^{4,5}, Rodrigo Nalio Ramos^{1,2,3}, Pamela Caudana^{1,2,3}, Jordan Denizeau^{1,2,3}, Christel Goudot^{1,2}, Jean-Michel Luccarini⁶, Anne Soudé⁶, Bruno Bournique⁶, Pierre Broqua⁶, Luigia Pace^{1,2#}, Sylvain Baulande⁷, Christine Sedlik^{1,2,3}, Jean-Pierre Quivy^{1,8,9}, Geneviève Almouzni^{1,8,9}, José Cohen^{4,5}, Elina Zueva^{1,2}, Joshua J. Waterfall^{1,3,10}, Sebastian Amigorena^{1,2‡*} and Eliane Piaggio^{1,2,3‡*}

1 Institut Curie, PSL Research University, F-75005 Paris, France.

2 INSERM U932, F-75005, Paris, France.

3 Institut Curie, Translational Research Department, F-75005 Paris, France.

4 Université Paris-Est, UMR S955, Université Paris-Est Créteil Val de Marne, Créteil, France.

5 INSERM, U955, Equipe 21, Créteil, France.

6 Inventiva, 50 rue de Dijon, 21121 Daix, France.

7 Institut Curie, Genomics of Excellence (ICGex) Platform, Institut Curie Research Center, Paris, France

8 Institut Curie, PSL Research University, CNRS, UMR3664, Equipe Labellisée Ligue contre le Cancer, Paris, France.

9 Sorbonne Universités, UPMC University Paris 06, CNRS, UMR3664, F-7005 Paris, France.

10 INSERM U830, F-75005 Paris, France.

[‡]S.Amigorena and E.Piaggio contributed equally to this paper.

[#] Current address : Armenise-Harvard Immune Regulation unit, IIGM, Candiolo (TO), 10060, Italy ; Candiolo Cancer Institute, FPO-IRCCS, Candiolo (TO), 10060, Italy.

*Correspondence:

Sebastian Amigorena INSERM U932, Institut Curie, 26, rue d'Ulm, 75005 Paris, France. Phone: 33 1 56 24 67 11; Fax: 33 1 44 07 07 85; E-mail: sebastian.amigorena@curie.fr

Eliane Piaggio INSERM U932, Institut Curie, 26, rue d'Ulm, 75005 Paris, France. Phone: 33 1 56 24 58 05; Fax: 33 1 44 07 07 85; E-mail: eliane.piaggio@curie.fr

Abstract

Tumor-infiltrating CD8⁺ T cells progressively lose functionality and fail to reject tumors. The underlying mechanism and re-programming induced by checkpoint blockers are incompletely understood. We show that genetic ablation or pharmacological inhibition of H3K9-methyl transferase Suv39h1 delays tumor growth and potentiates tumor rejection by anti-PD-1. In the absence of Suv39h1, anti-PD-1 induces alternative activation pathways allowing survival and differentiation of IFN- γ and GZMb-producing effector cells that express negative checkpoints, but do not reach final exhaustion. Their transcriptional program correlates with that of melanoma patients responding to immune-checkpoint blockade and identifies the emergence of cytolytic-effector tumor-infiltrating lymphocytes as a biomarker of clinical response. Anti-PD-1 favors chromatin opening in loci linked to T-cell activation, memory and pluripotency, but in the absence of Suv39h1, cells acquire accessibility in cytolytic effector loci. Overall, Suv39h1 inhibition enhances anti-tumor immune responses, alone or combined with anti-PD-1, suggesting that Suv39h1 is an “epigenetic checkpoint” for tumor immunity.

Introduction

Surface receptors that inhibit T cell function, or negative checkpoints, play a major role in tumor escape from immune responses. Similar to chronic antigen stimulation during viral infections, T cells inside tumors express high levels of inhibitory receptors and become dysfunctional or exhausted, losing their cytotoxic activity (van der Leun et al., 2020; Ahmadzadeh et al. 2009). Blocking certain inhibitory receptors with monoclonal antibodies (Abs) has become a major therapeutic tool in cancer patients. Treatment with CTLA-4 or PD-1 blocking Abs can induce potent immune responses against tumors and durable clinical responses. In mouse models, recent studies show critical roles for cytokines (including IL-27) and sequence-specific transcription factors (such as cMAF, TOX, T-bet, and EOMES) in the induction of T cell dysfunction (Chihara et al., 2018; Beltra et al., 2020). Gene expression programs associated with T cell dysfunction and with re-invigoration of T cell functions after checkpoint blockade have been identified in both humans and mice (Thommen et al., 2018; Chihara et al., 2018; Pauken et al., 2016).

These gene expression programs are intimately connected to precise control of chromatin dynamics, which determines the accessibility of genes and regulatory elements to transcription regulators (Yadav et al., 2018). Schematically, chromatin permissiveness to transcription is associated with chromatin modifiers including so-called writers and erasers, which biochemically modify histone tails, allowing the recruitment of effectors (readers) that modify the structure of the chromatin.

Suv39h1, a histone methyl transferase that promotes trimethylation of lysine 9 of H3 (H3K9me3)(Rea et al., 2000), plays critical roles in lymphocyte differentiation. In CD4⁺ T cells, Suv39h1 is associated with silencing of the IFN γ locus during Th2 differentiation (Allan et al., 2012). In the absence of Suv39h1 expression, Th2 cells differentiate, but fail to fully

commit to the Th2 fate, and start producing IFN γ *in vivo*. In CD8⁺ T cells, Suv39h1 silences the memory/stem cell gene expression program during differentiation of cytotoxic effectors. In the absence of Suv39h1 expression, CD8⁺ T cell effectors co-express memory genes, and display higher reconstitution potential after adoptive transfer (Pace et al., 2018). These results show that Suv39h1-induced heterochromatin dynamics plays a critical role during lymphocyte differentiation, and that chromatin modifiers control specific gene expression programs at precise stages of immune responses. Other epigenetic regulators, including EZH2 (Gray et al., 2017), DNA methyl-transferases (Youngblood et al., 2017) and histone chaperone CAF-1 (Ng et al., 2019) are also required to silence stem cell/memory programming during effector differentiation, indicating a general requirement for coordinated changes in chromatin dynamics.

Several recent studies have investigated chromatin accessibility changes during CD8⁺ T cell differentiation into memory, effector or exhausted phenotypes (Pauken et al. 2016; Sen et al. 2016; Philip et al., 2017). For the latter, transcriptomic and epigenomic changes that occur while T cells become exhausted in the context of chronic viral infection and cancer have been analyzed. A critical question in the field is to understand how blockade of checkpoints, such as anti-PD-1 treatment, reverses the dysfunction of exhausted CD8⁺ T cells. Recent studies have proposed that reversion of the exhausted phenotype can occur early during the onset of the exhaustion program, and that once this program is fully established it becomes irreversible, and that fully exhausted T cells can no longer respond to PD-1 blockade (Philip et al., 2017). Understanding the molecular basis and underlying chromatin dynamics for the establishment of the exhaustion program is a cornerstone with direct consequences for the development of therapeutic strategies in cancer and chronic infections.

In this study, we analyze the role of Suv39h1 in CD8⁺ T cell exhaustion and re-invigoration by PD-1 blockade in mouse tumors. Using both genetic and pharmacological approaches, we show that Suv39h1 inhibition overcomes tumor resistance to anti-PD-1 treatment. Immune phenotype and single cell RNAseq analysis show that Suv39h1-deficient TILs display phenotypic characteristics of exhausted cells, including high expression of multiple inhibitory checkpoints. However, the Suv39h1-defective TILs also express a strong IFN-I signature, and respond vigorously to PD-1 blockade, inducing potent tumor rejection and showing broader chromatin accessibility, in particular around genes linked to effector functions, as compared to wild type cells. We conclude that Suv39h1 expression in CD8⁺ T cells is instrumental for establishing an irreversible, anti-PD-1 resistant exhausted phenotype in tumors. As inhibition of Suv39h1 reverses T cell dysfunction and causes tumor rejection, Suv39h1 represents an actionable “epigenetic checkpoint” for T cell functions in cancer.

Results

Suv39h1 deficiency enhances solid tumor rejection in combination with anti-PD-1 Ab

To interrogate the role of Suv39h1 in T cell responses to cancer, we used a partially anti-PD-1 blockade resistant melanoma model, B16F10-OVA (in which the tumor cells express the surrogate tumor-antigen ovalbumin) grafted in WT or *Suv39h1*-KO mice. Tumor bearing

littermate WT and *Suv39h1*-KO mice were randomly assigned to two groups, treated or not with anti-PD-1 monoclonal Ab after establishment of the tumors (**Fig. 1A**). As expected, anti-PD-1 treatment induces a delay in tumor growth, but not complete rejection in WT mice (**Fig. 1B, 1C and 1D**). In *Suv39h1*-KO littermates, the growth of the tumor is similarly delayed, with a small number of tumor rejections (2/27), while treatment with anti-PD-1 induces complete tumor rejection in almost one-third of the mice (5/16, **Fig. 1B, 1C and 1D**). We conclude that *Suv39h1* deficiency in the host not only delays tumor growth to levels similar to anti-PD-1 administration, but also synergizes with anti-PD-1 treatment.

The *Suv39h1*-KO mice used here are constitutive knockouts affecting all cell types. To investigate the specific role of *Suv39h1*-deficient T cells in the observed tumor rejection phenotype, we adoptively transferred in vitro activated control WT and *Suv39h1*-KO OVA-specific T cell receptor (TCR) transgenic OT-1 cells to B6 mice bearing established EL4-OVA tumors (**Fig. S1A**). Mice that received *Suv39h1*-KO OT-1 T cells controlled tumor growth better than mice that received littermate WT OT-1 T cells (**Fig. S1B**), demonstrating that *Suv39h1* deficiency in CD8⁺ T cells augments their anti-tumor potential in the absence of any other *Suv39h1*-defective cell type.

To further understand the implication of *Suv39h1*-deficient CD8⁺ T cells in tumor-rejection, we investigated how *Suv39h1*-defective T cells behave in a Graft vs Host Disease/ Graft vs Leukemia (GvHD/GVL) model. Irradiated haplotype-matched B6xDBA/2 F1 mice (Hk2bxd; termed B6D2) received a transplant of C57BL/6 (H2kb) bone marrow, with or without *Suv39h1*-knockout (KO) or wild-type littermate (WT) T cells, before being challenged with P815-GFP murine mastocytoma cells (H2kd) (**Fig. S1C**). Both *Suv39h1*-KO and littermate WT T cells induced a modest increase in survival (10-30%), as compared to the control group that did not receive T cells (**Fig. S1D**). To determine if the mice died due to tumor or to GvHD development, tumor growth (**Fig. S1E and 1F**) and GvHD severity (**Fig. S1G and 1H**) were measured. While mice injected with WT T cells showed a high tumor incidence (more than 60% had detectable tumor cells) and developed mild GvHD, the mice injected with *Suv39h1*-KO T cells showed instead a lower tumor incidence (20%) and developed more severe GvHD. Indeed, while mice injected with WT T cells died from tumor development, the ones injected with *Suv39h1*-deficient T cells died from GvHD (78%) (**Fig. S1I**). Therefore, in this adoptive T cell transfer model *Suv39h1*-deficient T cells develop into much more potent effectors (that reject the tumor and attack the host) than their *Suv39h1*-proficient counterparts.

These two latter experiments (**Fig. S1**) suggest that the increased tumor control observed in *Suv39h1*-defective mice (**Fig. 1A-D**) could be attributed, at least partially, to an increased anti-tumor activity of *Suv39h1*-KO CD8⁺ T cells. Along these lines, the percentages of tumor-infiltrating myeloid cells (CD11b⁺ cells, cDC1, and cDC2 cells), CD4⁺ T cells, and NK and were similar in untreated WT and *Suv39h1*-KO animals, and were not significantly modified by the anti-PD-1 treatment (**Fig. S2A**); while the percentage and absolute number of CD8⁺ tumor-infiltrating lymphocytes (TILs) were increased in the *Suv39h1*-KO mice as compared to WT littermates, and were expanded further after treatment with anti-PD-1 Ab (**Fig. 1E**). The increase in CD8⁺ T cells was restricted to the tumor, as no such changes were observed in the tumor-draining lymph nodes (DLNs) (**Fig. S2B**). These results highlight the

link between increased CD8⁺ T-cell infiltration and tumor rejection in anti-PD-1 Ab treated *Suv39h1*-KO mice.

It has been previously described that Suv39h1 is a critical regulator of the transition of CD8⁺ T cells between the memory and effector differentiation states (Pace et al., 2018). Thus, we analyzed the proportions of naïve (CD44^{lo}CD62L^{hi}), central memory (CD44^{hi}CD62L^{hi}) and effector (CD44^{hi}CD62L^{lo}) CD8⁺ T cell subsets in blood (during tumor growth progression, at day 13), and in spleen, DLNs, and tumor (at sacrifice, day 20). We observed that in general, compared to WT mice, *Suv39h1*-KO littermates treated or not with anti-PD-1, showed lower proportions of naïve CD8⁺ T cells and higher proportions of effector and central memory subsets, in the three locations (**Fig. S2C-E**). In contrast, in the tumor, virtually no naïve CD8⁺ T cells were detected, and the main effect was observed in PD-1 treated *Suv39h1*-KO mice, in which the proportion of memory cells (CD44^{hi}CD62L^{hi}) was significantly lower, while both the proportion and the absolute number of effector CD8⁺ T cells were significantly higher (**Fig. 1F**). Therefore, the absence of Suv39h1 expression not only leads to higher CD8⁺ T-cell tumor-infiltration upon anti-PD-1 treatment, but also a change in the phenotype of the infiltrating cells, away from memory and towards a more pronounced effector phenotype.

***Suv39h1*-KO CD8⁺ TILs display enhanced functional capacity**

A vast body of literature shows that, upon tumor invasion, CD8⁺ T cells differentiate into an exhausted and unresponsive state in late-stage tumors (Phillip et al., 2017). Because tumors are rejected more efficiently in *Suv39h1*-defective mice treated or not with anti-PD-1, we hypothesized that the absence of Suv39h1 could delay or prevent exhaustion programs and together with checkpoint blockade could overcome dysfunctional states. To further investigate if *Suv39h1*-defective TILs are exhausted, we first analyzed the expression of negative-immune checkpoints, which represent a hallmark of exhaustion (Wherry and Kurachi, 2015). In *Suv39h1*-KO mice, treatment with anti-PD-1 caused a marked increase in the proportion of TILs expressing PD-1, TIM-3, LAG-3 and 2B4 (**Fig. 2A**) and of all combinations of these receptors (**Fig. 2B**), as well as other surface molecules associated with exhaustion, such as CD39, CD38 and CD101 (**Fig. S3A**), suggesting more advanced differentiation (Philip et al., 2017; Hudson et al., 2019; Zander et al., 2020). This increase was not observed in WT littermates treated in the same way.

To further study the effect of anti-PD-1 treatment on the activation state of *Suv39h1*-defective CD8⁺ TILs, we analyzed their effector functions, proliferation and survival, which have been previously described as impaired in exhausted T cells (Paley et al., 2012; Pauken et al., 2015). We observed that upon ex vivo stimulation CD8⁺ TILs from *Suv39h1*-KO mice expressed the highest levels of GZMb, a marker of cytotoxic function (**Fig. 2C**), readily produced IFN γ , as detected by ELISPOT (**Fig. 2D**), and responded to IFN γ , as indicated by the high expression of ISG15 (a hallmark gene of IFN-response) (**Fig. 2E**).

Furthermore, around 13% of CD8⁺ TILs from PD-1-treated *Suv39h1*-KO mice expressed higher levels of Ki67 (a marker of cycling cells, **Fig. 2F**). Nevertheless, increased cycling was not associated with augmented apoptosis, as suggested by the increased expression of BCL-2

(an anti-apoptotic molecule) (**Fig. 2G**) and small proportions of annexinV/7ADD⁺ cells (**Fig. 2H**), suggesting higher function and conserved viability. To further understand this intriguing observation, we analyzed the expression of T-box transcription factors EOMES and TBET, both crucial markers in effector and memory functions in T cells (Paley et al., 2012; Stelekati et al., 2018; Khan et al., 2019), as well as the HMG-box transcription factor TOX, primary regulator of exhaustion epigenetic program (Alfei et al., 2019). We observed similar levels of TOX in CD8⁺ TILs from all mice conditions, and increased levels of EOMES in anti-PD-1 treated *Suv39h1*-KO mice (**Fig. S3B**). Of interest, as cells get activated and enter into an exhaustion program, they upregulate the expression of Eomes; however, co-expression of EOMES with TBET has been associated with a rescue from a terminally exhausted state, as PD-1⁺EOMES⁺TBET⁺ cells retain effector functions. We observed that CD8⁺ PD-1⁺ TILs co-expressing EOMES and TBET were enriched in anti-PD-1 treated *Suv39h1*-KO mice (**Fig. 2I**). These results indicate the ability to rewire the transcriptional control of TBET and EOMES in CD8⁺ TILs in *Suv39h1* deficient mice after immunotherapy, independently of TOX expression. Thus, although *Suv39h1*-defective CD8⁺ TILs display features of exhausted cells (eg express high levels of negative checkpoints and EOMES), they are found in increased numbers (**Fig. 1E**), produce IFN γ and GZMb and importantly are not apoptotic, indicating enhanced poly-functionality and survival.

It has been recently described that anti-PD-1 Ab treatment may work not only by reinvigorating exhausted TILs, but also by inducing the proliferation of progenitor exhausted cells with memory/stem cell-like characteristics, as well as their differentiation into cytotoxic and short-lived, terminally exhausted cells resistant to anti-PD-1 therapy (Miller et al., 2019; Chen et al., 2019). We quantified the amount of progenitor and terminally exhausted T cells, identified as TCF1⁺TIM3⁻ or TCF1⁺TIM3⁺ cells respectively, among the memory CD8⁺PD-1⁺ TILs compartment (Miller et al., 2019). We observed that in the tumors of *Suv39h1*-KO mice, the proportion of stem-like progenitor exhausted CD8⁺ T cells was lower than in their WT littermates, and the percentage of terminally exhausted T cells was significantly higher in anti-PD-1 treated *Suv39h1*-KO CD8⁺ T cells compared with the WT mice (**Fig. 2J**), suggesting that in the absence of *Suv39h1* activity CD8⁺ TILs differentiate from a stem cell-like progenitor exhausted T cell to a more effector exhausted one. Similar results were obtained when using the cell surface marker SLAMF6 instead of the transcription factor TCF-1 (Miller et al., 2019) to quantify the precursor and the later effector populations (**Fig. S3C**). Recent studies in chronic viral infection demonstrated that the expression of the type I transmembrane glycoprotein CD101 subdivide the terminally exhausted population into two subgroups (Hudson et al., 2019). Stem cell-like progenitor exhausted TCF1⁺CD8⁺ T cells first differentiate into a transitory CD101⁺TIM3⁺ state marked by an effector-like profile displaying chemokine receptor CX3CR1, cytokines and GZMb expression, contribute to viral control and eventually progress to a terminally differentiated and dysfunctional CD101⁺TIM3⁺ state. Notably, Hudson et al. observed that PD-1 blockade increases the transitory cytolytic effector-like CD101⁺TIM3⁺ cells compared to stem-like CD8⁺ T cells. In the cancer context, we observed that anti-PD-1 treatment induced a subtle increase in the percentages of terminally exhausted CD101⁺TIM3⁺ cells in both WT and *Suv39h1*KO CD8⁺ TILs. The increase of transitory CD101⁺TIM3⁺ cells, in contrast, was stronger in *Suv39h1*-defective

mice relative to the control littermates (**Fig. 2K**). These results indicate that in the absence of SUV39H1, anti-PD-1 treatment increases the proliferative and effector T cell differentiation by enhancing the conversion to transitory exhausted CD101-TIM3⁺ T cells.

scRNAseq analysis of tumor-infiltrating CD8⁺ T cells

To further characterize the impact of Suv39h1 on TIL programming, we performed single cell RNA sequencing (scRNA-seq) of CD8⁺ TILs isolated from B16F10-OVA tumors of *Suv39h1*-KO and littermate WT mice treated or not with anti-PD-1 (**Fig. 3A**). In total, 21646 cells (1524 to 5953 cells per sample) were merged, and 8 clusters were defined, which are visualized using UMAP in **Fig. 3B** (see methods and **Fig. S4** for bioinformatics pipeline details). Figure 3 shows the signatures used to define cluster identities (**Fig. 3C**), as well as key exemplifying genes (violin plots, **Fig. 3D**; and heatmap, **Fig. 3E**). Fig S4D-E shows additional information used to define each cluster. In more detail, cluster 1 and 2 were composed of cells bearing high memory signatures: “C1-memory 1” characterized by high expression of *Lef1* and *Il7r*; and “C2-memory 2” by *Id3*, *Ikzf2/Helios* and killer cell lectin-receptors (*Klra1* and *Klra6*); cluster 3, “C3-early activated” included cells with a signature of recent TCR-engagement, as featured by the expression of *Nr4a1* and *Dusp2*; cluster 4, “C4-IFN- α response” expressed an IFN- α -induced gene signature; cluster 5, “C5-effector cytolytic”, shared similarities with the previously described short-lived effector T cell cytolytic cluster required to control chronic viral infection containing the chemokine receptor *Cx3cr1*, genes associated with cytotoxicity (*Gzma*, *Klrg1* and *Gzmb*) and the transcription factors *Zeb2* and *Klf3* (Guo et al., 2018; Azizi et al., 2018; Zander et al., 2019); cluster 6, “C6-progenitor exhausted” was composed of cells highly expressing *Ccr7*, *Id3*, *Slamf6*, *Cd200* and *Cd74* indicative of progenitor stem cell- like exhausted cells; cluster 7, “C7-terminally exhausted” showed a late exhausted signature and highly expressed the pathognomonic genes *Havcr2*, *Gzmb*, and *Mt1* (encoding metallothionein-1), which has been described to promote T-cell dysfunction during cancer (Singer et al., 2017); and cluster 8, “C8-cycling” expressed a cell cycle signature and the characteristic active cell cycle phase genes *Top2a* and *Mki67*. Altogether, these results identify a high heterogeneity among CD8⁺ TIL populations, likely reflecting a broad functional specialization.

Suv39h1-deficient TILs show an IFN- α response signature and a higher cytolytic potential upon PD-1 blockade

To further investigate how treatment with anti-PD-1 Ab affects reprogramming of CD8⁺ TILs in WT and *Suv39h1*-KO mice, we then explored the transcriptomic differences of the clusters between conditions. All clusters were present in each of the four analyzed conditions, but in different proportions. Thus, we first performed downsampling, so as to analyze the same amount of cells in each condition (randomly sampling 4097 cells from each condition to match the smallest one, n=16388 total cells after downsampling), and then quantified the changes in the proportions of cells belonging to each cluster from treated and untreated, littermate WT and *Suv39h1*-KO mice. As shown in **Figure 4A** and **4B**, CD8⁺ TILs from

littermate WT untreated mice contained the highest proportions of memory and progenitor exhausted cells compared to all the other conditions. Upon anti-PD-1 treatment, these populations seemed to evolve into an exhausted state. Distinctively, in untreated conditions *Suv39h1*-defective TILs were characterized by higher proportions of “IFN-responding” and “exhausted” cells than WT cells. Upon anti-PD-1 treatment, *Suv39h1*-KO CD8⁺T cells comprised the highest frequencies of early activated, effector cytolytic and IFN-responsive cells. These results suggest that along the activation/differentiation program of anti-tumor T cells, *Suv39h1* dependent silencing of the IFN-I response and of pathways of the exhaustion program, imposes an epigenetic barrier that prevents re-programing of TILs towards a terminally exhausted program by anti-PD-1. Moreover, our data indicate that in the absence of *Suv39h1*, CD8⁺ TILs are poised to more effectively respond to TCR-activation and to become highly cytolytic upon PD-1-blockade, underlying the increased tumor rejection compared to WT mice.

The anti-PD-1 response signature of *Suv39h1*-deficient CD8⁺ T cells discriminates response to anti-PD-1 in melanoma patients

We then asked whether the signature of *Suv39h1*-KO CD8⁺ T cells that increase after anti-PD-1 in the mice is relevant to human cancer. To address this question, we first interrogated whether our data correlated with available published signatures from scRNAseq of CD8⁺ T cells from melanoma patients responding or not to immune checkpoint blockade (Sade-Feldman et al., 2018). To that end, we first confirmed that the “responder” and “non-responder” signatures from the original paper correspond to distinct subpopulations of cells in the human dataset (**Fig. S5A, S5B and Fig. 4C**). To compare mice and human anti-PD-1 responses, we computed ortholog-matched signatures of each experimental group (littermate WT, littermate WT + anti-PD-1, KO, and KO + anti-PD-1) and quantified them on the reprocessed human melanoma cohort UMAP (**Fig. 4D**). We observed that the KO + anti-PD-1 signature best matched with the “responder” signature from the original study, and that they were strongly positively correlated ($R = 0,54$, $p < 2.2e-16$) (**Fig. 4E**). Interestingly, the KO + anti-PD-1 signature was also anti-correlated with the “non-responder” signature ($R = -0,39$, $p < 2.2e-16$). Finally, we also noticed an enrichment of the KO + anti-PD-1 signature coming from our mice data in responding patients ($p=4.8 \times 10^{-12}$) (**Fig. S5C**), suggesting that our KO + anti-PD-1 signature could be a potential biomarker of response to immune checkpoint blockade (ICB) therapy.

We next used our mouse scRNAseq data to identify the specific subtype of CD8⁺ T cell response induced by the treatment in the responder patients. To that end, we first plotted signatures of our different conditions (littermate WT, littermate WT + anti-PD-1, KO, KO + anti-PD-1) (**Fig. 4F**) and compared them with four previously published melanoma ICB response signatures (Sade-Feldman et al., 2018; Hugo et al., 2016; Riaz et al., 2017 and Liu et al., 2019) (**Fig. 4G**). While each of these four previous studies differ with regards to detailed patient clinical characteristics, RNAseq profiling techniques and analytical approaches, we observed that across the four studies, the human signatures of response to immunotherapy were consistently associated to the cytolytic effector, TCR activation and IFN type I clusters,

which are also those upregulated in the mouse KO + anti-PD-1 CD8⁺ T cells, and to a lesser degree to an increase of a fraction of “terminally exhausted” cells.

Overall, the transcriptional program induced by anti-PD-1 in the absence of Suv39H1 activity is associated with human T cells responding to PD-1 blockade and clearly links the emergence of effector CD8⁺ T cell subpopulations to the effectiveness of immune checkpoint blockade.

Suv39h1-deficiency enhances chromatin accessibility induced by anti-PD-1

To investigate the effect of anti-PD-1 reprogramming on chromatin accessibility in WT and *Suv39h1*-KO T cells, we next used *Assay for Transposase-Accessible Chromatin with high throughput sequencing* (ATAC-seq). CD8⁺ TILs were FACS-sorted from tumors growing in WT and *Suv39h1*-KO mice, treated or not with anti-PD-1. Accessible regions were first identified by calling ATAC-peaks for each condition. Tens of thousands of peaks were detected in each sample, with numbers systematically higher for anti-PD-1-treated cells, both in WT and *Suv39h1*-KO CD8⁺ T cells, relative to untreated samples (**Fig. 5A**). To get quantitative insight into changes caused by anti-PD-1 treatment, we first compared treated samples directly to their untreated genotype-matched counterparts. An ATAC peak (identified in either condition) was considered modulated if it harbored twice or more sequencing reads (normalized for sequencing depth) as compared to the corresponding counterpart (**Fig. 5B, left panel**). Strikingly, with this approach no regions emerge as enriched in anti-PD-1 untreated relative to treated samples. On the contrary, anti-PD-1 treatment induces a widespread increase in chromatin accessibility in both WT and *Suv39h1*-KO populations. In WT cells, almost 6000 regions at least double their ATAC-signal, as compared to their untreated counterparts. In *Suv39h1*-KO cells, the effect of treatment is even more dramatic, with 35000 genomic regions gaining accessibility (almost half of all identified ATAC peaks in KO cells). In WT CD8⁺ TILs, the majority (68%, 4009/5866) of treatment-induced regions (T-peaks) are shared with *Suv39h1*-KO T-peaks (**Fig. 5B, left panel**). ATAC signal density plots generated for 20% of the most variable T-peaks (**Fig. 5B, right panel**) reveal well-defined clusters: (i) *Suv39h1*-KO -specific, (ii) WT-specific, and (iii) common to both genotypes. To cross-compare accessibilities of identified treatment-specific peaks in all four conditions, we plotted the distribution of ATAC signal in peaks for each cluster separately. As expected, average signals in WT or *Suv39h1*-KO treatment-specific peaks are higher, as compared to the corresponding untreated counterparts (**Fig. 5C**). Importantly, a stronger signal in *Suv39h1*-KO cells on shared T-peaks suggests that they are more accessible in a higher proportion of cells, as compared to WT. These results indicate that anti-PD-1 treatment promotes chromatin accessibility, and that this effect is more pronounced in the absence of Suv39h1.

To reveal biological signatures associated with anti-PD-1 treatment, we next assigned treatment-specific peaks to their nearest genes. We observed that the majority of genes assigned to T-peaks in WT cells are shared with *Suv39h1*-KO (**Fig. 5D, left panel**), but conversely, the majority of T-peaks in *Suv39h1*-KO cells are not differentially accessible in WT cells. Signature enrichment analysis showed that anti-PD-1 treatment leads to an increase

in chromatin accessibility in genomic loci linked to T cell memory, pluripotency and activation (TCR pathway, IL-2 pathway, IFN γ -response, and exhaustion), in both WT and *Suv39h1*-KO CD8⁺ T cells (**Fig. 5D, right panel**). The progenitor signature, however, is more enriched in WT, while the IFN γ - and IFN-I signatures are more enriched in KO cells. Moreover, multiple effector signatures (cytolytic, terminally differentiated, as well as cell cycle) are uniquely associated with T-peaks in *Suv39h1*-defective cells. **Figure 5D**, lower panel shows loci of representative TCR mediated activation gene *EGr1*, effector genes (*Cx3cr1* and *Gzmb*) and IFN-stimulated gene *Mx1*, that become more accessible in *Suv39h1*-KO cells after anti-PD-1 treatment as compared to other conditions. These results suggest that altogether, anti-PD-1 treatment favors chromatin opening in genomic loci linked to T cell activation, memory and pluripotency, but in a *Suv39h1*-KO context cells acquire preferential accessibility in functional IFN-related and cytolytic effector loci as compared to WT cells.

To investigate the differences between WT and *Suv39h1*-KO populations after anti-PD-1 treatment, we next compared chromatin opening in the two populations. We only retained ATAC regions harboring twice or more reads and, importantly, called as peaks uniquely open in one, but not the other population after the treatment (**Fig. 5E, upper panel**). Of these peaks, around 1500 in WT and 1700 in KO are identified as condition-specific (see density plots in **Fig. 5E** with selected adjacent genes). Peaks uniquely accessible in treated WT cells (when compared to treated KO cells), are equally accessible in untreated WT population, (see ATAC signal distribution in **Fig. 5E, lower panel**). Only 3% of them are modulated by the treatment, suggesting that these are mostly stably opened regions in WT TILs. Peaks specific to treated *Suv39h1*-KO cells (compared to treated WT cells), are also accessible in untreated KO samples, although over half of them (58%) respond to the treatment with a strong increase in accessibility (**Fig. 5E, lower panel**). Therefore, in the absence of Suv39h1, a series of chromatin regions, mostly treatment-sensitive, fail to remain closed. As ATAC-regions are typically associated with active or poised regulatory elements (Buenrostro, et al., 2013), these results collectively suggest that Suv39h1 may contribute to the regulation of chromatin opening at cis-regulatory elements that support differentiation of T cells into functional cytolytic effectors upon re-activation.

Pharmacological inhibition of Suv39h1 phenocopies the genetic defect

Since genetic deficiency for Suv39h1 increases the response to anti-PD-1 treatment, we next evaluated the effect of ETP-69, a pharmacological inhibitor of Suv39h1 activity. ETP-69, which is not strictly specific for Suv39h1 (it also inhibits G9A, another mono- and dimethylase of H3K9) has been previously reported to function in mice (Overman et al., 2014; Snigdha et al., 2016). Here, we evaluated its effect in combination therapy with PD-1-blockade. For this, C57BL/6 mice bearing established B16F10-OVA tumors were treated daily with ETP-69 combined or not with anti-PD-1 (**Fig. 6A**). ETP-69 and anti-PD-1 administered as monotherapies induced a clear delay in tumor growth, and the combination of both was more effective than either of the single agents (**Fig. 6B and 6C**). The increased efficiency of the combination treatment was ETP-69 dose-dependant (**Fig. S6A and S6B**).

We conclude that pharmacological inhibition of Suv39h1 augments the efficacy of anti-PD-1 blockade in this tumor model.

We observed that frequencies and absolute numbers of CD8⁺ TILs were increased in ETP-69 treated mice, as compared to control groups, especially after treatment with anti-PD-1 (**Fig. 6D**). Similar to the results obtained in Suv39h1-deficient mice, ETP-69 alone or in combination with anti-PD-1 induced an increase in the proportion of effector CD8⁺ TILs, paralleled by a reduction in the proportion of memory TIL populations (**Fig. 6E**). In blood and secondary lymphoid organs, ETP-69 treatment lead to a reduction of naïve CD8⁺ T cells and increased proportions of central and effector memory subsets (**Fig. S6A**). Furthermore, CD8⁺ TILs from ETP-69 treated mice expressed multiple inhibitory checkpoint receptors (**Fig. 6F and 6G**), and higher proportions of GZMb and IFN γ upon restimulation (**Fig. 6H**), and of Ki67⁺ cells (**Fig. 6I**). Finally, as observed for Suv39h1-KO mice treated with anti-PD-1, a higher proportion of CD8⁺ PD-1⁺ TILs from ETP-69 + anti-PD-1 treated mice co-expressed EOMES and TBET (**Fig. 6J**). We conclude that, similar to the Suv39h1-genetic defect, treatment of WT tumor-bearing mice with the Suv39h1 inhibitor ETP-69 reduces tumor growth, especially in combination with anti-PD-1. The inhibitor also enhances tumor infiltration by effector CD8⁺ T cells that express high levels of multiple inhibitory checkpoints but with an increased effector cytotoxic phenotype. Therefore, pharmacological inhibition phenotypically and functionally phenocopies the genetic defect of Suv39h1.

Discussion

In the tumor microenvironment, conditioned by hypoxia, nutrient shortage and tumor factors, “chronic” activation of CD8⁺ T lymphocytes progressively leads to loss of their effector functions and unresponsiveness to further stimulation, a process often referred to as “final exhaustion”. Although the signaling pathways involved in the induction of exhaustion are incompletely understood, the transcriptional programs expressed in exhausted cells have been analyzed in some details. Induction and silencing of hundreds of genes are under the control of critical transcription factors such as IRF4, cMAF, NFAT, TOX, EOMES and T-bet and others (Martinez et al., 2015; Chihara et al., 2018). Similar to any gene expression program, transcriptional regulation of exhaustion and re-invigoration upon immune checkpoint blockade can only be promoted under a precise control of chromatin accessibility at the corresponding loci. Here, we identify Suv39h1, the main H3K9 tri-methylase and a hallmark of facultative and constitutive heterochromatin (Nielsen et al., 2001; Wiencke et al., 2008), as a key epigenetic positive regulator of functional exhaustion.

Based on our results, we propose a working model in which, Suv39h1 contributes to progression of TILs along the exhaustion pathway through heterochromatin-mediated silencing of IFN-I gene expression programs and pathways downstream of TCR-signaling, inhibiting the deployment of an effector program. Thus, as cells become exhausted, silencing of these gene expression programs establishes an epigenetic barrier that prevents effective reprogramming by PD-1 blockade. In the absence of Suv39h1, this epigenetic barrier is incomplete and TCR-triggering in memory/effector cells leads to an alternative activation pathway that allows survival and differentiation into highly cytolytic effectors without

reaching final exhaustion. This in turn allows more effective re-invigoration of exhausted TILs by anti-PD-1 Ab, and more efficient tumor rejection

How then does Suv39h1 repress TCR activation, terminal differentiation and ISG expression programs? Our previous work showed that several stem cell/memory related genes display reduced levels of H3K9me3 deposition in *Suv39h1*-KO T cells, suggesting that they are direct targets of Suv39h1 (Pace et al., 2018). Chromatin analyses in TILs, however, are complicated because of reduced cell numbers and heterogeneity among individual mice. Interestingly, enhanced IFN-I signature genes are also overexpressed in hematopoietic stem cells (Wu et al., 2018), suggesting a shared link between the mechanisms that control the two gene expression programs. The link could be direct, such as through deposition of the same histone marks (including H3K9me3) at memory and ISGs loci. H3K9me3 could also control ISGs indirectly, for example through regulation of expression of transposable elements (TEs), which in turn drive IFN-signaling. Indeed, Suv39h1 was shown to control expression of several families of TEs in fibroblasts and RNA from TEs can be sensed in the cytosol and induce activation of STING and IFN-I (Sidler et al., 2014).

To investigate the mechanisms of Suv39h1 action, we sequenced single cell transcriptomes from over 21000 infiltrating CD8⁺ T cells from B16F10-OVA tumors in WT, or *Suv39h1*-defective mice, treated or not-treated by anti-PD-1 Ab. Our single cell analysis captured a high heterogeneity of CD8⁺ TILs, encompassing lymphocytes undergoing different states of activation: cycling, memory, memory effectors, progenitor exhausted, recently-TCR activated, IFN-responding, and cytolytic effectors subpopulations; but as expected no naïve cells. The frequency of cycling cells detected by this technique was not increased in anti-PD-1-treated mice (WT or *Suv39h1*-KO, **Fig. 4B**), while, at least in the KO, anti-PD-1 induced increased proportions of Ki67-positive cells. This could be due to limitations of the available transcriptomic signatures of cycling, as in our single cell analysis, the cluster of cycling cells includes cells in different phases of the G2M and S phases, which seem not to change in a systematic way among the different conditions (**Fig. S4B and S4C**). The changes observed in the relative proportion of cells belonging to the other clusters indicate that during the anti-tumor response, Suv39h1 represses IFN-I signaling, and part of the exhaustion program, restraining the cells in a more memory/progenitor exhausted state, and T cell reinvigoration induced by PD-1 blockade drives these cells into a terminally exhausted program. However, in the absence of this epigenetic barrier imposed by Suv39h1, TCR-mediated reactivation is restored, and leads to highly cytolytic effectors with anti-tumor potential. Consistent with this working model, signatures from scRNAseq CD8⁺ T cells from melanoma patients that respond to immune checkpoint blockers correlated strongly with the transcriptomic signature of PD-1-treated *Suv39h1*-KO CD8⁺ T cells. Reciprocally, the PD-1-treated *Suv39h1*-KO signature was enriched in responding patients, indicating that this signature could potentially be used as biomarker of response in melanoma patients. Furthermore, the high granularity of CD8⁺ T cell populations characterized in scRNAseq analysis of the mouse data, allowed us to identify which were the specific CD8⁺ T subpopulations responding to ICB in patients, using as input published melanoma ICB response signatures obtained from single cell or bulk RNA sequencing. Of note, this analysis identified that, as in PD-1-treated *Suv39h1*-KO mice, response to immune checkpoint blockade was consistently associated to the emergence of

cytolytic effector and TCR activation-; a feature not previously highlighted in patients-, and also IFN type I signatures, as previously described (Liu et al., 2019).

Our results identify a critical epigenetic regulator of exhaustion. They also establish a clear link between IFN-I, early activation, cytolytic effectors and re-programing of progenitor exhausted cells. This link may be particularly relevant to the multiple immunotherapy approaches based on inducing IFN-I responses in the tumor environment, including cytolytic viruses, STING agonists, and DNA-demethylating agents. Since Suv39h1 genetic deficiency or pharmacological inhibition both re-activate anti-tumor immune responses, and promote re-programing by anti-PD-1, the role of Suv39h1 in this process must be at least partially non-redundant. By analogy to other non-redundant immunosuppressive proteins whose inhibition unleashes anti-tumor immune responses (often referred to as “immune checkpoints”), Suv39h1 can be considered as an “epigenetic immune checkpoint”. Should the role of Suv39h1 be conserved in human T cells, its blockade would open new perspectives for the epigenetic manipulation of anti-tumor T cell responses in the clinic.

Acknowledgments

We thank Virginie Dangles-Marie, Celine Daviaud, Isabelle Grandjean, Mikael Garcial and Cedrik Paurchad, the mouse facility technicians and flow cytometry core at Institut Curie. We thank Nathalie Amzallag for technical assistance. This work was supported by the ANR-14-CE16-009 (Programme ANR Innovation biomedical DS0404, 2014), Institut National de la Santé et de la Recherche Médicale, Labex DCBIOL (ANR-10-IDEX-0001-02 PSL and ANR-11-LABX0043), SIRIC INCa-DGOS-Inserm_12554. P.G. is supported by a PhD fellowship from Ligue Nationale contre le Cancer at Université Paris Descartes (Paris V). P.C. was supported by a fellowship from the International PhD program of Institut Curie. The authors declare no competing financial interests.

Author contributions

L.L.N., C.S., L.P., S.A., and E.P. conceptualization. L.L.N., J.C., C.S., S.A., and E.P. designed experiments. L.L.N., E. Z., A.T., P.C., R.R., J.D., Q.Z., Z.L., B.K., and X.H. performed the experiments. M.Y., E. Z., L.L.N. analyzed ATACseq data. L.L.N., P.G., C.G., and J.W. analyzed scRNAseq data. J.-M.L., A.S., B.B., P.B., performed ETP-69 compound synthesis and pharmacokinetics studies. L.L.N., E. Z., S.A., and E.P. wrote the manuscript, with all authors contributing to writing and providing feedback. S.A., and E.P. supervision. J.-P. Q, G.A., S.A., and E.P. funding acquisition.

Declaration of conflict of interest

S. Amigorena, J. Waterfall and E. Piaggio are shareholders in Mnemo Therapeutics. P. Broqua and Anne Soude are employees and shareholders in Inventiva Pharma. The other authors declare no competing interests.

References

- Ahmadzadeh, M., Johnson, L.A., Heemskerk, B., Wunderlich, J.R., Dudley, M.E., White, D.E., Rosenberg, S.A. (2009). Tumor antigen-specific CD8 T cells infiltrating the tumor express high levels of PD-1 and are functionally impaired. *Blood* 114, 1537-1544.
- Alfei, F., Kanev, K., Hofmann, M., Wu, M., Ghoneim, H.E., Roelli, P., Utzschneider, D.T., Hösslin, M., et al. (2019). TOX reinforces the phenotype and longevity of exhausted t cells in chronic viral infection. *Nature* 571, 265-269.
- Allan, R.S., Zueva, E., Cammas, F., Schreiber, H.A., Masson, V., Belz, G.T., Roche, D., Maison, C., Quivy, J.-P., Almouzni, G., et al. (2012). An epigenetic silencing pathway controlling T helper 2 cell lineage commitment. *Nature* 487, 249–253.
- Azizi, E., Carr, A.J., Plitas, G., Cornish, A.E., Konopacki, C., Prabhakaran, S., Nainys, J., Kenmin, Wu., et al. (2018). Single-Cell Map of Diverse Immune Phenotypes in the Breast Tumor Microenvironment. *Cell* 174, 1293-1308.
- Beltra, J.-C., Manne, S., Abdel-Hakeem, M.S., Kurachi, M., Giles, J.R., Chen, Z., Casella, V., et al. (2020). Developmental Relationships of Four Exhausted CD8+ T Cell Subsets Reveals Underlying Transcriptional and Epigenetic Landscape Control Mechanisms. *Immunity* 52, 1-17.
- Buenrostro, J. D., Giresi, P. G., Zaba, L. C., Chang, H. Y., Greenleaf, W. J. (2013). Transposition of native chromatin for fast and sensitive epigenomic profiling of open chromatin, DNA- binding proteins and nucleosome position. *Nat. Methods* 10, 1213–1218.
- Butler, A., Hoffman, P., Smibert, P., Papalexi, E., and Satija, R. (2018). Integrating single-cell transcriptomic data across different conditions, technologies, and species. *Nat. Biotechnol.* 36, 411–420.
- Chen, Z., Zhicheng, J., Ngiow, S.F., Manne, S., Cai, Z., Huang., A.C., Johnson, J., Staupe, R.P., et al. (2019). TCF-1-Centered Transcriptional Network Drives an Effector versus Exhausted CD8 T Cell-Fate Decision. *Immunity* 51, 1-16.
- Chihara, N., Madi, A., Kondo, T., Zhang, H., Acharya, N., Singer, M., Nyman, J., Marjanovic, N.D., Kowalczyk, M.S., Wang, C., et al. (2018). Induction and transcriptional regulation of the co-inhibitory gene module in T cells. *Nature* 558, 454–459.
- Finak, G., McDavid, A., Yajima, M., Deng, J., Gersuk, V., Shalek, A.K., Slichter, C.K., Miller, H.W., McElrath, M.J., Prlic, M., et al. (2015). MAST: a flexible statistical framework for assessing transcriptional changes and characterizing heterogeneity in single-cell RNA sequencing data. *Genome Biol.* 16.
- Gray, S.M., Amezquita, R.A., Guan, T., Kleinstein, S.H., and Kaech, S.M. (2017). Polycomb Repressive Complex 2-Mediated Chromatin Repression Guides Effector CD8 + T Cell Terminal Differentiation and Loss of Multipotency. *Immunity* 46, 596–608.
- Guo, X., Zhang, Y., Zheng, L., Zheng, C., Song, J., Zhang, Q., Kang, B., Liu, Z., Jin, L., Xing, R., et al. (2018). Global characterization of T cells in non-small-cell lung cancer by single-cell sequencing. *Nat. Med.* 24, 978-985.

Hudson, W.H., Gensheimer, J., Hashimoto, M., Wieland, A., Valanparambil, R.M., Li, P., et al. (2019). Proliferating Transitory T Cells with an Effector-like Transcriptional Signature Emerge from PD-1+ Stem- like CD8+ T Cells during Chronic Infection. *Immunity* 51, 1043-1058.

Hugo, W., Zaretsky, J.M., Sun, L., Song, C., Homet Moreno, B., Hu-Lieskovan, S., Berent-Maoz, B., Pang, J., et al. (2017). Genomic and Transcriptomic Features of Response to Anti-PD-1 Therapy in Metastatic Melanoma. *Cell* 165, 35-44.

Khan, O., Giles, J.R., McDonald, S., Manne, S., Ngiow, S.F., Patel, K.P., Werner, M.T., Huang, A.C., et al. (2019). TOX transcriptionally and epigenetically programs CD8+ T cell exhaustion. *Nature* 571, 211-218.

Leclerc, M., Naserian, S., Pilon, C., Martin, G.H., Pouchy, G., Dominique, C., Belkacemi, Y., Charlotte, F., et al. (2016). Control of GVHD by regulatory T cells depends on TNF produced by T cells and TNFR2 expressed by regulatory T cells. *Blood* 128 (12), 1651–1659.

Liu, D., Schilling, B., Liu, D., Sucker, A., Livingsstone, E., Jerby-Arnon, L., Zimmer, L., Gutzmer, R., (2019). Integrative molecular and clinical modeling of clinical outcomes to PD1 blockade in patients with metastatic melanoma. *Nat. Med.* 25, 1916-1927.

Martinez, G.J., Pereira, R.M., Aijo, T., Kim, E.Y., Marangoni, F., Pipkin, M.E., Togher, S., Heissmeyer, V., et al. (2015). The Transcription Factor NFAT Promotes Exhaustion of Activated CD8+ T Cells. *Immunity* 42, 265-278.

Miller, B.C., Sen, D.R., Abosy, R.A., Bi, K., Virkud, Y.V., LaFleur, M.W., Yates, K.B., Lako, A., et al. (2019). Subsets of exhausted CD8+ T cells differentially mediate tumor control and respond to checkpoint blockade. *Nat. Immunol.* 20, 326-336.

Naserian, S., Leclerc, M., Thiolat, T., Pilon, C., Le Bret, C., Belkacemi, Y., Maury, S., Charlotte, F., and Cohen, J.L. (2018). Simple, Reproducible, and Efficient Clinical Grading System for Murine Models of Acute Graft-versus-Host Disease. *Front. Immunol.* 9.

Nielsen, A.L., Oulad-Abdelghani, M., Ortiz, J.A., Remboutsika, E., Chambon, P., Losson, R. (2001). Heterochromatin formation in mammalian cells: interaction between histones and HP1 proteins. *Mol. Cell.* 7, 729-739.

Ng, C., Aichinger, M., Nguyen, T., Au, C., Najar, T., Wu, Lin., Mesa, K.R., Liao, W., Quivy J.-P., Hubert, B., Almouzni, G., et al. (2019). The histone chaperone CAF-1 cooperates with the DNA methyltransferases to maintain Cd4 silencing in cytotoxic T cells. *Genes Dev.* 33, 669-683.

Overman, L.E., Baumann, M., Nam, S., Horne, D., Jove, R., Xie, J. and Kowolik, C. (2014). Preparation of Epipolythiodioxopiperazine ETP derivatives for treatment of cancer. WO2014066435 A1.

- Pace, L., Goudot, C., Zueva, E., Gueguen, P., Burgdorf, N., Waterfall, J.J., Quivy, J.-P., Almouzni, G., and Amigorena, S. (2018). The epigenetic control of stemness in CD8⁺ T cell fate commitment. *Science* 359, 177–186.
- Paley, M.A., Kroy, D.C., Odorizzi, P.M., Johnnidis, J.B., Dolfi, D.V., Barnett, B.E., Bikoff, E.K., Robertson, E.J., Lauer, G.M., Reiner, S.L., et al. (2012). Progenitor and Terminal Subsets of CD8⁺ T Cells Cooperate to Contain Chronic Viral Infection. *Science* 338, 1220–1225.
- Pauken, K.E., and Wherry, E.J. (2015). Overcoming T cell exhaustion in infection and cancer. *Trends Immunol.* 36, 265–276.
- Pauken, K.E., Sammons, M.A., Odorizzi, P.M., Manne, S., Godec, J., Khan, O., Drake, A.M., Chen, Z., Sen, D.R., Kurachi, M., et al. (2016). Epigenetic stability of exhausted T cells limits durability of reinvigoration by PD-1 blockade. *Science* 354, 1160–1165.
- Philip, M., Fairchild, L., Sun, L., Horste, E.L., Camara, S., Shakiba, M., Scott, A.C., Viale, A., Lauer, P., Merghoub, T., et al. (2017). Chromatin states define tumour-specific T cell dysfunction and reprogramming. *Nature* 545, 452–456.
- Qiu, X., Hill, A., Packer, J., Lin, D., Ma, Y.-A., and Trapnell, C. (2017). Single-cell mRNA quantification and differential analysis with Census. *Nat. Methods* 14, 309–315.
- Rea, S., Eisenhaber, F., Ponting, C.P., Allis, C.D., and Jenuwein, T. (2000). Regulation of chromatin structure by site-specific histone H3 methyltransferases. *406*, 7.
- Riaz, N., Havel, J.J., Makarov, V., Desrichard, A., Urba, W.J., Sims, J.S., Hodi, F.S., Martin-Algarra, S., et al. (2017). Tumor and Microenvironment Evolution during Immunotherapy with Nivolumab. *Cell* 171, 934–949.
- Sade-Feldman, M., Yizhak, K., Bjorgaard, S.L., Ray, J.P., de Boer C.G., Jenkins, R.W., et al. (2018). Defining T Cell States Associated with Response to Checkpoint Immunotherapy in Melanoma. *Cell* 175, 998–1013.
- Satija, R., Farrell, J.A., Gennert, D., Schier, A.F., and Regev, A. (2015). Spatial reconstruction of single-cell gene expression data. *Nat. Biotechnol.* 33, 495–502.
- Sen, D.R., Kaminski, J., Barnitz, R.A., Kurachi, M., Gerdemann, U., Yates, K.B., Tsao, H.-W., Godec, J., LaFleur, M.W., Brown, F.D., et al. (2016). The epigenetic landscape of T cell exhaustion. *Science* 354, 165–169.
- Sidler, C., Woycicki, R., Li, D., Wang, B., Kovalchuk, I., and Kovalchuk, O. (2014). A role for SUV39H1-mediated H3K9 trimethylation in the control of genome stability and senescence in WI38 human diploid lung fibroblasts. *Aging* 6, 545–563.
- Snigdha, S., Prieto, G.A., Petrosyan, A., Loertscher, B.M., Dieskau, A.P., Overman, L.E., and Cotman, C.W. (2016). H3K9me3 Inhibition Improves Memory, Promotes Spine Formation, and Increases BDNF Levels in the Aged Hippocampus. *J. Neurosci.* 36, 3611–3622.

- Stelekati, E., Chen, Z., Manne, S., Kurachi, M., Ali, M.-A., Lewy, K., Cai, Z., Nzingha, K., McLane, L.M., Hope, J.L., et al. (2018). Long-Term Persistence of Exhausted CD8 T Cells in Chronic Infection Is Regulated by MicroRNA-155. *Cell Rep.* 23, 2142–2156.
- Thommen, D.S., Koelzer, V.H., Herzig, P., Roller, A., Trefny, M., Dimeloe, S., Kiialainen, A., Hanhart, J., Schill, C., Hess, C., et al. (2018). A transcriptionally and functionally distinct PD-1⁺ CD8⁺ T cell pool with predictive potential in non-small-cell lung cancer treated with PD-1 blockade. *Nat. Med.* 24, 994-1004.
- van der leun, A.M., Thommen, D.S., Schumacher, T.N. (2020). CD8⁺ T cell states in human cancer: insights from single- cell analysis. *Nat. Rev. Cancer* 20, 218-232.
- Wherry, E.J., and Kurachi, M. (2015). Molecular and cellular insights into T cell exhaustion. *Nat. Rev. Immunol.* 15, 486–499.
- Wiencke, J.K., Zheng, S., Morrison, Z. and Yeh, R-F. (2008). Differentially expressed genes are marked by histone 3 lysine 9 trimethylation in human cancer cells. *Oncogene* 27, 2412-2421.
- Wu, X., Dao Thi, V.L., Huang, Y., Billerbeck, E., Saha, D., Hoffmann, H.-H., Wang, Y., Silva, L.A.V., Sarbanes, S., Sun, T., et al. (2018). Intrinsic Immunity Shapes Viral Resistance of Stem Cells. *Cell* 172, 423-438.e25.
- Yadav, T., Quivy J.-P., Almouzni, G. (2018). Chromatin plasticity: A versatile landscape that underlies cell fate and identity. *Science* 361, 1332-1336.
- Youngblood, B., Hale, J.S., Kissick, H.T., Ahn, E., Xu, X., Wieland, A., Araki, K., West, E.E., Ghoneim, H.E., Fan, Y., et al. (2017). Effector CD8 T cells dedifferentiate into long-lived memory cells. *Nature* 552, 404–409.
- Zander, R., Schauder, D., Xin, G., Nguyen, C., Wu, X., Zajac, A. and Cui, W. (2020). CD4⁺ T Cell Help Is Required for the Formation of a Cytolytic CD8⁺ T Cell Subset that Protects against Chronic Infection and Cancer. *Immunity* 53, 1-15.
- Zappia, L., and Oshlack, A. (2018). Clustering trees: a visualization for evaluating clusterings at multiple resolutions. *GigaScience* 7.
- Zemmour, D., Zilionis, R., Kiner, E., Klein, A.M., Mathis, D., and Benoist, C. (2018). Single-cell gene expression reveals a landscape of regulatory T cell phenotypes shaped by the TCR. *Nat. Immunol.* 19, 291–301.

Figure legends

Figure 1. Suv39h1 deficiency inhibits tumor growth in combination with anti-PD-1 Ab

(A) Graphical representation of model system of experimental groups, including littermates WT and *Suv39h1*-KO mice receiving B16F10-OVA melanoma cells followed by PBS or anti-PD-1 Ab.

(B) Tumor growth kinetics in B16F10-OVA bearing littermate WT and *Suv39h1*-KO mice receiving PBS or anti-PD-1 Ab. Pooled results from three independent experiments are shown. Numbers refer to rejected tumors out of total mice analyzed. Black arrows indicate time point of initial PBS or anti-PD-1 Ab injection.

(C) Tumor growth kinetics. Data is represented as mean.

(D) Tumor volumes in cm³ (at day of sacrifice, day 20).

(E) Frequency (%) and quantification (number) of CD8⁺ TILs (CD45⁺TCRb⁺CD4⁻).

(F) Representative dot plots showing the frequency of memory and effector CD8⁺ TILs from B16F10-OVA tumors, frequency (%) and quantification (number).

p values were calculated using Mann-Whitney test. *p<0.05; **p<0.01; ***p<0.001; ****p<0.0001.

See also Figures S1 and S2.

Figure 2. PD-1 blockade in *Suv39h1*-KO CD8⁺ TILs modifies their exhaustion program and enhances their effector capacity

(A) Representative histogram and frequency (%) of inhibitory receptors (PD-1⁺, TIM-3⁺, LAG-3⁺ and 2B4⁺) on CD8⁺ TILs from B16F10-OVA tumors.

(B) Pie chart of co-expression (PD-1⁺, TIM-3⁺, LAG-3⁺ and 2B44⁺) on CD8⁺ TILs from B16F10-OVA tumors.

(C) Representative histogram and frequency (%) of GZMb⁺ cells among CD8⁺ TILs. Cells were re-stimulated in vitro with PMA and ionomycin for 4 hr. (GZMb: Granzyme b).

(D) Blood cells from mice were re-stimulated ex vivo with OVA-I_{SIINFEKL} peptide. The number of OVA-specific T cells producing IFN-γ per 2,5x10⁵ blood cells was determined by ELISPOT analysis.

(E) Representative histogram and frequency (%) of ISG15⁺ among CD8⁺ TILs from B16F10-OVA tumors.

(F) Representative histogram and frequency (%) of Ki67⁺ among CD8⁺ TILs from B16F10-OVA tumors.

(G) Representative histogram and frequency (%) of BCL-2⁺ among CD8⁺ TILs from B16F10-OVA tumors.

(H) Frequency (%) of Annexin V⁺ 7ADD⁻ among CD8⁺ TILs from B16F10-OVA tumors.

(I) Representative contour plots and frequency (%) of TBET⁺EOMES⁺ among CD8⁺ PD-1⁺ TILs from B16F10-OVA tumors.

(J) Representative contour plots and frequency (%) of progenitor exhausted (TCF1⁺TIM-3⁻) and late exhausted (TCF1⁻TIM-3⁺) among CD8⁺ PD-1⁺ TILs from B16F10-OVA tumors.

(K) Representative histogram and frequency (%) of transitory (CD101⁻) and exhausted (CD101⁺) among CD8⁺ PD-1⁺ TCF1⁻TIM-3⁺ TILs from B16F10-OVA tumors.

A representative experiment out of two is shown. p values were calculated using Mann-Whitney test. *p<0.05; **p<0.01; ***p<0.001; ****p<0.0001.

See also Figures S3.

Figure 3. Identification of multiple CD8⁺ TIL populations by single cell RNA sequencing

(A) Scheme of the overall study design. Single-cell RNA sequencing was applied to CD8⁺ TILs isolated from littermate WT and *SUV39h1*-KO mice receiving B16F10-OVA melanoma cells followed by PBS or anti-PD-1 Ab.

(B) UMAP plot with clusters differentiated by colour demonstrating eight distinct CD8⁺ TILs clusters based on gene expression differences for 21646 passing quality control cells. Each dot corresponds to one single cell.

(C) Feature plots and violin plots showing distribution of signature scores indicated by cluster.

(D) Violin plots showing expression distribution of representative genes for each cluster.

(E) Heatmap showing Z scores for the average expression of selected genes within the eight clusters.

See also Figures S4.

Figure 4. PD-1 blockade in *SUV39h1*-KO CD8⁺ TILs induces a transcriptomic effector phenotype also found in responder melanoma patients

(A) UMAP plot of 4097 cells for each of the four analyzed conditions after downsampling (on the top) and the corresponding density plots (on the bottom).

(B) Heatmap of proportion and numeric value of the downsampled 4097 cells for each of the four conditions within the eight clusters.

(C) Feature plots of human melanoma CD8⁺ TILs showing responder and not responder signature score from scRNAseq published dataset (Sade-Feldman et al., 2018).

(D) Feature plots of human melanoma CD8⁺ TILs showing distribution of signature scores from littermate WT and *Suv39h1*-KO treated or not with anti-PD-1 dataset conditions.

(E) Correlation between transcriptomic signatures from *Suv39h1*-KO mice treated with anti-PD-1 and the responder and not responder melanoma patients (Sade-Feldman et al., 2018) calculated with Person correlation coefficient.

(F) Feature plots of murine CD8⁺ TILs (Figure 3B) highlighting distribution of signature scores of littermate WT and *Suv39h1*-KO treated or not with anti-PD-1 dataset conditions.

(G) Enrichment of the transcriptomic signature of genes upregulated in published melanoma ICB responders projected in murine CD8⁺ TILs UMAP (Figure 3B).

See also Figures S5.

Figure 5. *Suv39h1*-deficiency enhances anti-PD-1 induced chromatin opening at TCR-, cytolytic-, and IFN α - responsive sites

(A) Number of chromatin accessible regions in CD8⁺ TILs of littermate WT and *Suv39h1*-KO mice treated or not with anti-PD-1.

(B) ATAC-seq regions in littermate WT and *Suv39h1*-KO modulated by anti-PD-1 treatment. Venn diagram showing anti-PD-1 treatment modulated peaks in littermate WT, *Suv39h1*-KO, or both (overlap) (middle). Chromatin accessibility heat map grouped by modulated peaks by anti-PD-1 treatment in CD8⁺ TILs of littermate WT, *Suv39h1*-KO, or both (bottom).

(C) Distribution of anti-PD-1 induced ATAC-seq signals in CD8⁺ TILs littermate WT and *Suv39h1*-KO CD8⁺ TILs.

(D) Venn diagram showing number of genes adjacent to anti-PD-1 induced ATAC-seq peaks in littermate WT and *Suv39h1*-KO CD8⁺ TILs (top). Selected signatures enriched in anti-PD-1 induced adjacent peaks open in littermate WT and *Suv39h1*-KO CD8⁺ TILs determined through hypergeometric test alternative greater (middle). Representative ATAC-seq tracks showing accessibility peaks across the loci of *Egr1*, *Mx1*, *Cx3cr1* and *Gzmb* for littermate WT and *Suv39h1*-KO treated or not with anti-PD-1 CD8⁺ TILs (bottom).

(E) Chromatin accessibility heat map grouped by unique differentially accessibility regions in CD8⁺ TILs of littermate WT + anti-PD-1 and *Suv39h1*-KO + anti-PD-1 (top). Distribution of unique anti-PD-1 signals in CD8⁺ TILs of littermate WT + anti-PD-1 and *Suv39h1*-KO + anti-PD-1.

All ATAC-seq data are representative of two biologically independent pooled samples.

Figure 6. Pharmacological inhibition of *Suv39h1* potentiates tumor rejection by anti-PD-1 Ab

(A) Graphical representation of model system of experimental groups, including C57BL/6 mice receiving B16F10-OVA melanoma cells followed by ETP-69 oral treatment, PBS or anti-PD-1 Ab injection.

(B) Tumor growth kinetics represented as means of one representative experiment out of 2; with n=X o X mice per group. Black arrows indicate time of initial ETP-69 or vehicle control dose administration and anti-PD-1 Ab injection.

(C) Tumor volumes in cm³ (on the day of sacrifice, day 19).

(D) Frequency (%) and quantification (number) of CD8⁺ TILs (CD45⁺TCRb⁺CD4⁻).

(E) Frequency (%) of memory and effector CD8⁺ TILs from B16F10-OVA tumors.

(F) Representative histogram and frequency (%) of inhibitory receptors (PD-1⁺, TIM-3⁺, LAG-3⁺ and 2B4⁺) on CD8⁺ TILs from B16F10-OVA tumors.

(G) Pie chart of co-expression (PD-1⁺, TIM-3⁺, LAG-3⁺ and 2B4⁺) on CD8⁺ TILs from B16F10-OVA tumors.

(H) Representative histogram and frequency (%) of GZMb⁺ and IFNγ⁺ cells among CD8⁺ TILs. Cells were re-stimulated in vitro with PMA and ionomycin for 4 hr.

(I) Representative histogram and frequency (%) of Ki67⁺ among CD8⁺ TILs from B16F10-OVA tumors.

(J) Frequency (%) of TBET⁺EOMES⁺ among CD8⁺ PD-1⁺ TILs from B16F10-OVA tumors.

A representative experiment out of two is shown. p values were calculated using Mann-Whitney test. *p<0.05; **p<0.01; ***p<0.001; ****p<0.0001. See also Figure S8.

See also Figures S6.

Supplementary figure legends

Figure S1. *Suv39h1*-KO CD8⁺ T cells show higher anti-tumoral effects than WT CD8⁺ T cells. Related to Figure 1.

(A) EL4-OVA tumor model. Experimental design. Littermate WT or *Suv39h1*-KO OT-I cells (CD45.1⁺) were activated with IL-2 and OVA-I peptide for 6 days and adoptively transferred (i.v.) to congenic CD45.2⁺ recipient mice bearing EL4-OVA tumor.

(B) Tumor growth kinetics. Numbers refer to rejected tumors out of total mice analyzed.

(C) P815-GFP tumor model. P815-GFP cells were injected into irradiated B6D2F1 recipient mice grafted with bone marrow cells (n=6), supplemented with littermate WT (n=10) or *Suv39h1*-KO (n=10) CD3⁺ T cells. The experiment was performed twice and the resulting survival (D), tumoral incidence (E-F) and clinical score (G-H) data were pooled. The pie chart (I) represent the proportion of mice dead of leukemia (grey) or GvHD (white). Kaplan-Meier survival curves were compared using log-rank test. For analysis of GvHD clinical grading curves, AUC was calculated for each mouse, and then Student t test or 1-way ANOVA with post hoc analysis was performed depending on number of comparatives. ns, nonsignificant. * p<0.05; **** p<0.0001. **** p<0.0001

Figure S2. *Suv39h1* is critical for peripheral CD8⁺ T cell differentiation to a memory like phenotype. Related to Figure 2.

(A) Frequency (%) of CD11b⁺, cDC1 (CD45⁺CD64⁺F4/80⁺Lin⁻(CD19, NKp46, TCRb) MHCII⁺CD11c⁺CD26⁺XCR1⁺CD127a⁻), cDC2 (CD45⁺CD64⁺F4/80⁺Lin⁻(CD19, NKp46, TCRb) MHCII⁺CD11c⁺CD26⁺XCR1⁻CD127a⁺) and NK cells (CD45⁺TCRb⁻NK1.1⁺), in B16F10-OVA tumors at day 20 after tumor inoculation.

(B) Frequency (%) and quantification (number) of CD8⁺ in DLN at day 20 after tumor inoculation (CD45⁺TCRb⁺CD4⁻).

(C) Representative contour plots and frequency (%) of CD8⁺ naive, central memory and effector T cells in blood from tumor bearing mice at day 12 after tumor inoculation.

(D) Representative dot plots and frequency (%) of CD8⁺ naive, central memory and effector T cells in spleen from tumor bearing mice at day 20 after tumor inoculation.

(E) Representative dot plots and frequency (%) of CD8⁺ naive, central memory and effector T cells in DLN from tumor bearing mice at day 20 after tumor inoculation.

p values were calculated using Mann-Whitney test. *p<0.05; **p<0.01; ***p<0.001; ****p<0.0001.

Figure S3. *Suv39h1*-KO mice treated with anti-PD-1 show CD8⁺ TILs with altered effector and exhaustion phenotypes. Related to Figure 2.

(A) Representative histogram and frequency (%) of surface receptors (CD39⁺, CD38⁺ and CD101⁺) on CD8⁺ TILs from B16F10-OVA tumors.

(B) Representative histogram and frequency (%) of transcription factors EOMES and TOX on CD8⁺ TILs from B16F10-OVA tumors.

(C) Representative contour plots and frequency (%) of progenitor exhausted (SLAMF6⁺TIM-3⁻) and late exhausted (SLAMF6⁻TIM-3⁺) among CD8⁺ PD-1⁺ TILs from B16F10-OVA tumors.

Figure S4. Characterization of CD8⁺ TILs clusters by scRNAseq. Related to Figure 3 and Figure 4.

(A) UMAP plot displaying 16 clusters based on gene expression differences for 21646 passing quality control cells (resolution 0.7). Clusters with matched identities and equivalent CD8⁺ TILs proportions among littermate WT and *Suv39h1*-KO treated or not with anti-PD-1 were merged resulting in a final of 8 clusters (see Fig.3B).

(B) UMAP plot showing cell cycle phases.

(C) Feature and violin plots showing expression of cell cycle phase genes.

(D) Feature plots showing expression of indicated genes.

(E) Heatmap from single-cell analysis of 21646 cells from littermate WT and *Suv39h1*-KO treated or not with anti-PD-1 grouped into clusters. The top 15 genes differentially expressed for each cluster are shown in y axis. Heatmap colour scheme is based on Z-score distribution.

Figure S5. Transcriptomic correlation between human and *Suv39h1*-KO mice responses to immune checkpoint blockade. Related to Figure 4.

(A) To more faithfully compare the human and mice signature of CD8⁺ TILs we first reprocessed the human CD45⁺ single cell data extracted from Sade-Feldman et al. 2018, to generate a new dataset containing only CD8⁺ T cells. Left: UMAP plot displaying scRNAseq of all CD45⁺ from melanoma patient responders and non responders to ICB treatment, before

eliminating non CD8⁺ T cells. Right: feature plots showing expression of indicated genes used to conserve CD8⁺ T cells.

(B) UMAP plot displaying CD8⁺ T cells from melanoma patients and identifying CD8⁺ T cells from patients responding or not to ICB treatment (Sade-Feldman et al., 2018).

(C) Violin plots showing the enrichment of signature of genes upregulated in *Suv39h1*-KO + aPD-1 signature projected in CD8⁺ T cells from melanoma patient responders and non responders to ICB treatment (Sade-Feldman et al., 2018).

Figure S6. Dose effect of Suv39h1 inhibition combined with immunotherapy. Related to Figure 6.

(A) Graphical representation of model system of experimental groups, including C57BL/6 mice receiving B16F10-OVA melanoma cells followed by ETP-69 oral treatment (10 mg/kg or 20 mg/kg), PBS or anti-PD-1 Ab injection.

(B) Tumor growth kinetics represented as mean of one independent experiment.

(C) Tumor volumes in cm³ (on the day of sacrifice, day 20).

(D) Frequency (%) of CD8⁺ naive, central memory and effector T cells in blood, DLN and spleen from tumor bearing mice at day 12 or day 20 after tumor inoculation.

A representative experiment out of two is shown. p values were calculated using Mann-Whitney test. *p<0.05; **p<0.01.

Materials and Methods

Mice

C57BL/6J males (H-2^b) and C57BL/6J female hybrids B6D2F1 [B6xDBA/]2 F1 (H-2^{bxd}) mice were obtained from Charles River Laboratories and used at 8-10 weeks of age. *Suv39h1*^{tm1Jnw} C57BL/6J (*Suv39h1*-KO) mice were kindly provided by T. Jenuwein as previously described (Peters et al., 2001), were backcrossed with C57BL/6J mice for at least nine generations. C57BL/6J-Tg(*TcrαTcrβ*)1100Mjb/J mice (OT-I), and B6.SJL-*Ptprca* *Pepcb*/BoyJ (CD45.1) mice were purchased from Jackson lab. OT-I mice were crossed with CD45.1 mice to obtain OT-I/CD45.1 mice. Animal care and use for this study were performed in accordance with the recommendations of the European Community (2010/63/UE) for the care and use of laboratory animals. Experimental procedures were specifically approved by the ethics committee CEEA-IC #118 and the Ministère de l'enseignement supérieur, de la recherche et de l'innovation (APAFIS#12325_20171124123634-v2) in compliance with the international guidelines.

GVHD and leukemia model

Recipient B6D2F1 female mice received a 10-Gy irradiation followed by retro-orbital infusion of 5×10^6 bone marrow cells (C57BL/6J) + 1×10^6 CD3⁺ T cells from WT littermate or *Suv39h1*-KO mice + 2×10^4 mastocytoma cells P815-GFP derived from DBA/2 (H-2^d) mice (gift from Dr. B. Salomon). Total splenocytes and lymph nodes suspension cells were prepared for CD3⁺ T cells enrichment using pan T cells isolation kit (Miltenyi). Bone marrow suspension were prepared using leg bones. Control groups were constituted of irradiated mice receiving only bone marrow or bone marrow and P815-GFP cells. GVHD and Leukemia was evaluated two times per week. GVHD was evaluated as previously described (Leclerc et al., 2016; Naserian et al., 2018), and leukemia by flow cytometry (GFP⁺ H-2K^d + cells) and tumor bearing eyes.

In vivo tumor progression and immunotherapy

Half million of melanoma cells B16F10 expressing OVA (B16-OVA) or one million of EL4 lymphoma cells expressing OVA (EL4-OVA) were injected subcutaneously (s.c.) into the right flank of mice. Mice were randomly assigned a treatment group and tumor volume determined by caliper measurements. Anti-PD-1 Ab (clone RMP1-14, BioXcell), was administered intraperitoneally at 150 ug/ 20 g mice weight per dose on days 6-7, 11, 15 and 18-19.

Flow cytometry

For flow cytometric analysis, blood cells were harvested on day 12 post tumor implantation while DLN, spleen and tumor were harvested at day 19-20 post tumor implantation. Red blood cells were lysed with hypotonic buffer, single-cell suspensions were prepared in PBS 0.5% BSA and 2 mM EDTA (FACS buffer). Tumors were digested in 2 ml of CO₂ Independent medium (GIBCO) containing 0,1mg/ml DNase I and 0,1mg/ml Liberase TL (Roche) at 37°C for 30 min in agitation. Samples were transferred to C tubes (Miltenyi Biotec) for mechanical dissociation with GentleMACS and cell suspension was then filtered with a 100um cell strainer. Mononuclear cells were recovered from Percoll gradient (GE Healthcare Life Science) from 40% to 75% interface, washed and resuspended in FACS buffer. Live/dead cell discrimination was performed using Live/Dead Fixable Aqua Dead Cell Stain Kit (Life Technologies) or DAPI (Life Technologies) and Fc receptors were blocked with the CD16/CD32 (clone 2.4.G2) mAb (BD). Staining was performed with Abs listed in Supplementary Table 1. For intracellular staining of cytokines, cells were re-stimulated with phorbol 12-myristate 13-acetate (PMA, 20ng/ml) and 1 ug/ml of ionomycin (Sigma-Aldrich) for 4 hours at 37°C in the presence of GolgiStop and GolgiPlug (BD Biosciences). Cell surface labelling was done according to the experiment at 4°C and intracellular staining was done using a fixation/permeabilization kit (eBioscience/Thermo Fischer) according to the manufacturer's instructions. All data acquisition was done using an LSRFortessa (BD) and analyzed using FlowJo software (TreeStar).

Adoptive transfer

Total splenocytes and lymph nodes suspension cells of WT littermate and *Suv39h1*-KO CD45.1 OT-1 mice were cultured for 6 days in vitro with anti-CD3 (10 µg/mL), anti-CD28 (1 µg/mL) mAbs (BD) and OVA peptide (SIINFEKL, 1mg/ml) supplemented with rhIL-2 (100U/mL Proleukin, Novartis) in RPMI medium (GIBCO), with 2-mercaptoethanol, Pen-Strep, L-Glutamine (LifeTechnologies), and 10% FCS (Biosera). Three million of treated cells/mouse were injected i.v. into previously EL4-OVA tumor inoculated C57BL/6J mice and measured for tumor volume growth.

Analysis of OVA-specific CD8⁺ T cells

Blood cells were harvested on day 12 post tumor implantation. 300,000 cells were plated per well in plates (MAIPS4510, Millipore) coated with anti-murine IFN-γ Ab (Diacclone) and cultured overnight at 37°C in RPMI medium (GIBCO), with 2-mercaptoethanol, Pen-Strep, L-Glutamine (LifeTechnologies), and 10% FCS (Biosera) with OVA peptide (SIINFEKL, 1mg/ml) as antigen for restimulation. The IFN-γ producing cell were detected with biotinylated anti IFN-γ (Diacclone) followed by streptavidin-alkaline phosphatase (Mabtech) and revealed using the appropriate substrate (Biorad). Dots were counted with an ELISPOT Reader System ELR02 (AID, Germany).

Sample preparation for Single-cell RNA-seq and ATAC-seq

Suv39h1-KO and littermate WT mice were injected with B16-OVA tumor cells as previously described. On day 20, tumors were processed with Liberase and DNase I, stained with DAPI, CD45.2, TCRb, CD8, CD19, NK1.1, F4/80 and sorted on an Aria (BD) by gating on live, CD45.2⁺, (CD19, NK1.1, F4/80 negative cells) and CD8⁺ on PBS 0.04% BSA.

Single-cell RNA-seq

Cells were loaded on a 10x Chromium instrument (10x Genomics) and libraries were prepared using a Single Cell 3' Reagent Kit (V2 chemistry) (10x Genomics) according to manufacturer's protocol. Briefly, the initial step consisted in performing an emulsion where individual cells were isolated into droplets together with gel beads coated with unique primers bearing 10x cell barcodes, unique molecular identifiers (UMI), and poly (dT) sequences. Reverse transcription reactions were engaged to generate barcoded full-length cDNA followed by the disruption of emulsions using the recovery agent and cDNA clean up with DynaBeads MyOne Silane Beads (Thermo Fisher Scientific). Amplification of bulk cDNA was achieved using GeneAmp PCR System 9700 with 96-Well Gold Sample Block Module (Applied Biosystems) (98 °C for 3 min; cycled 14x: 98 °C for 15 s, 67 °C for 20 s, and 72 °C for 1 min; held at 4 °C). A final clean up step of amplified cDNA product was performed using the SPRI select Reagent Kit (Beckman Coulter). Indexed libraries were constructed following these steps: (1) fragmentation, end repair and A-tailing; (2) size selection with SPRI select beads; (3) adaptor ligation; (4) post-ligation cleanup with SPRI select beads; (5) sample

index PCR and final cleanup with SPRI select beads. Library quantification and quality assessment were achieved by Qubit fluorometric assay (Invitrogen) using dsDNA HS (High Sensitivity) Assay Kit and Bioanalyzer Agilent 2100 System using a High Sensitivity DNA chip. Indexed libraries were tested for quality, equimolarly pooled and sequenced on an Illumina HiSeq2500 using paired-end 26x98bp as sequencing mode. By using a full Rapid flow cell, coverage was around 100M reads per sample corresponding to 100000 reads per cell.

Single-cell RNA-seq analysis

Single-cell expression was analyzed using the Cell Ranger Single Cell Software Suite (v2.0.1) to perform quality control, sample de-multiplexing, barcode processing, and single-cell 3' gene counting. Sequencing reads were aligned to the mm10 transcriptome using the Cell Ranger suite with default parameters. CCA merging was performed using Seurat CCA (alignment score 0.87) and accounting for the 1000 most variable genes, and taking into account the 15 first CCs for downstream analysis (Butler et al., 2018). A total of 21646 single cells were analyzed. Further analysis was performed in R (v3.4) using the Seurat package (v2.3) (Satija et al., 2015). The gene-cell-barcode matrix of the samples was log-transformed and filtered based on the number of genes detected per cell (any cell with less than 400 genes or more than 6000 genes per cell was filtered out). Any cell with more than 6% of mitochondrial UMI (Unique Molecular Identifiers) counts and more than 50% of ribosomal UMI was filtered out. Genes detected in at least three cells were included. Cells were then scaled to a total of 1×10^4 molecules.

Clusters were identified using the “Find_Clusters” function in Seurat with a resolution parameter of 0.7. Clustree analysis was performed using Clustree R package (Version 0.2.2) (Zappia and Oshlack, 2018). 16 clusters were initially defined, and are visualized using UMAP in Fig. S4A). To simplify the analysis, some clusters which shared defined signatures and which did not evidently change among the different conditions were grouped as follow: original clusters 1, 3, 6, 7 and 11, corresponded to cycling cells in the G1/S and G2/M phase (Fig. S4B-C), were merged into one cluster (cluster 8 “cycling cells”, Fig. 3B); and original clusters 0, 8, 12, 13 and 14 (in Fig. S4A) which shared a “late exhaustion” signature, were merged together (as cluster 7 “late exhausted”, Fig. 3B).

Unique cluster-specific genes were identified by running the Seurat “Find_All_Markers” function using the MAST framework (Version 3alpha) (Finak et al., 2015). Contaminating cells were removed using the expression of Tyrobp, H2-Eb1, Apoe and Hbb-b.

Signature scores were computed using the Seurat function “AddModuleScore” using the gene signature of interest. This function calculates for each individual cell the average expression of each gene signature, subtracted by the aggregated expression of control gene sets. All analyzed genes are binned into 25 bins based on averaged expression, and for each gene of the gene signature, 100 control genes are randomly selected from the same bin as the gene. Featureplots were plotted using minimum and maximum cutoff values for each feature were respectively quantile 3 and quantile 97. UMAP was used for dimension reduction and

SimplePPT was used to learn the graph. Data is available at GEO (accession numbers XXX). Scripts used to perform this analysis are available on GitHub (<https://github.com/p-gueguen/XXX>).

ATAC-seq

Chromatin profiling was performed by ATAC-seq as described in Buenrostro et al. In brief, 50,000 cells per sample were washed in cold PBS and lysed. Transposition reaction was performed at 37°C for 30 minutes and DNA was purified with MinElute PCR purification kit (Qiagen). Transposed DNA was amplified for 5 cycles and additional PCR cycles were evaluated by real time PCR. Libraries were sequenced on Novaseq 6000 using 1xSp-Flow Cell (Illumina). A total of 130 to 210x10⁶ paired reads were generated per sample.

ATAC-seq data analysis

1) *Alignment, peak calling, and visualization*: ATAC-Seq sequencing reads were aligned to the mouse reference genome mm10 using BWAMEM (bwa-0.7.15, opt -k 19 -T 30 -M). Only properly paired uniquely mapped reads were kept for further analysis (samtools -f 0x2 -q 30). Peaks were called using MACS2 v2.1.2 with default parameters and a 5% FDR threshold. ATAC-seq signal tracks were generated using bamCoverage (deeptools-v2.5.3, --binSize 10 - -normalizeUsing BPM), and visualized in Integrative Genomics Viewer (IGV) software. 2) *Comparison between conditions*: Two strategies of peak calling were performed : 1) to detect individual peaks in each separate condition, peaks were called on merged replicates versus genome background; 2) to detect modulated peaks between conditions, peaks were called on merged replicates using 1 condition as treatment and another as control; further analysis on modulated peaks were filtered either by 1) only real peaks identified above by the peak caller, 2) fold-enrichment ≥ 2 , or 3) uniquely identified in treatment condition during individual peak calling. 3) *Signature enrichment analysis*: ATAC peaks were annotated using HOMER::annotatePeaks to nearest TSS gene. Signature enrichment analysis was applied on selected signatures using hypergeometric test alternative greater and BH adjusted p-value < 0.01 .

Statistical analysis

Unpaired t test and Kruskal-Wallis post-test was used for statistical analysis. All statistical analyses were performed with Prism software (Graphpad Software, Inc.). Symbols used *, $p < 0.05$; **, $p < 0.01$ ***, $p < 0.001$, n.s.: not significant.

Supplementary Table 1

Antibody	Color	Clone	Reference	Supplier
BCL-2	PE	BCL/10C4	633508	Biolegend

CD4	BUV737	RM4-5	564933	BD
CD4	BUV395	GK1.5	563790	BD
CD8a	BUV395	53-6.7	563786	BD
CD8a	BUV737	53-6.7	564297	BD
CD8a	PE-CF594	53-6.7	562315	BD
CD11b	APC-Cy7	M1/70	101261	Biolegend
CD11b	PE-Cy7	M1/70	101216	Biolegend
CD11c	PE-Texas Red	N418	MCD11C17	Invitrogen
CD19	BV650	6D5	115541	Biolegend
CD19	PE-Cy7	6D5	115520	Biolegend
CD26	FITC	H194-112	137806	Biolegend
CD38	PerCP-Cy TM 5.5	90/CD38	562770	BD
CD39	PE-Cy7	24DMS1	25-0391-82	Invitrogen
CD44	BV605	IM7	103047	Biolegend
CD44	BV650	IM7	103049	Biolegend
CD44	BUV737	IM7	564392	BD
CD44	PE	IM7	553134	BD
CD45.2	Alexa Fluor 700	104	109822	Biolegend
CD45.2	BUV737	104	564880	BD
CD62L	APC	MEL-14	553152	BD
CD62L	BV711	MEL-14	740660	BD
CD62L	FITC	MEL-14	533150	BD
CD64	APC	X54-5/7.1	139306	Biolegend
CD101	Alexa Fluor 647	307707	564473	BD
CD127 (IL-7R α)	BV421	A7R34	135024	Biolegend
CD122 (IL-2R β)	PE-Cy7	TM- β 1	123216	Biolegend
CD172a (SIRP alpha)	PerCP-eFluor 710	P84	46-1721-82	Invitrogen
CD223 (LAG-3)	BV421	C9B7W	125221	Biolegend
CD244.2 (2B4)	FITC	eBio244F4	11-2441-82	eBioscience
CD279 (PD-1)	BV785	29F.1A12	135225	Biolegend
CD335 (NKp46)	PE-Cy7	29A1.4	25-3351-82	eBioscience
CD366 (Tim-3)	APC	RTM3-23	119706	Biolegend
CD366 (Tim-3)	PE	RTM3-23	134004	Biolegend
EOMES	PE-eFluor 610	Dan11mag	61-4875-80	eBioscience

EOMES	PerCP-eFluor 710	Dan11mag	46-4875-82	eBioscience
F4/80	BV785	BM8	123141	Biolegend
F4/80	PE-Cy7	BM8	25-4801-82	eBioscience
Granzyme B	Pacific Blue	GB11	515408	Biolegend
H-2K[b]	Alexa Fluor 647	AF6-88.5	562832	BD
ISG15	PE	F-9	sc-166755	Sta Cruz Bio.
Ki67	PE	B56	556027	BD
MHC Class II (I-A/I-E)	eFluor 450	M5/114.15.2	48-5321-82	Invitrogen
NK1.1	PE-Cy5	PK136	108716	Biolegend
NK1.1	PE-Cy7	PK136	552878	BD
SLAMF6 (Ly-108)	BV421	13G3	740090	BD
Tbet	PE-Cy7	4B10	644824	Biolegend
TCF1	Alexa Fluor 488	C63D9	6444S	Biolegend
TCRb	APC-Cy7	H57-597	109220	Biolegend
TOX	PE	TXRX10	12-6502-82	Invitrogen
XCR1	BV650	ZET	148220	Biolegend

Fig.1

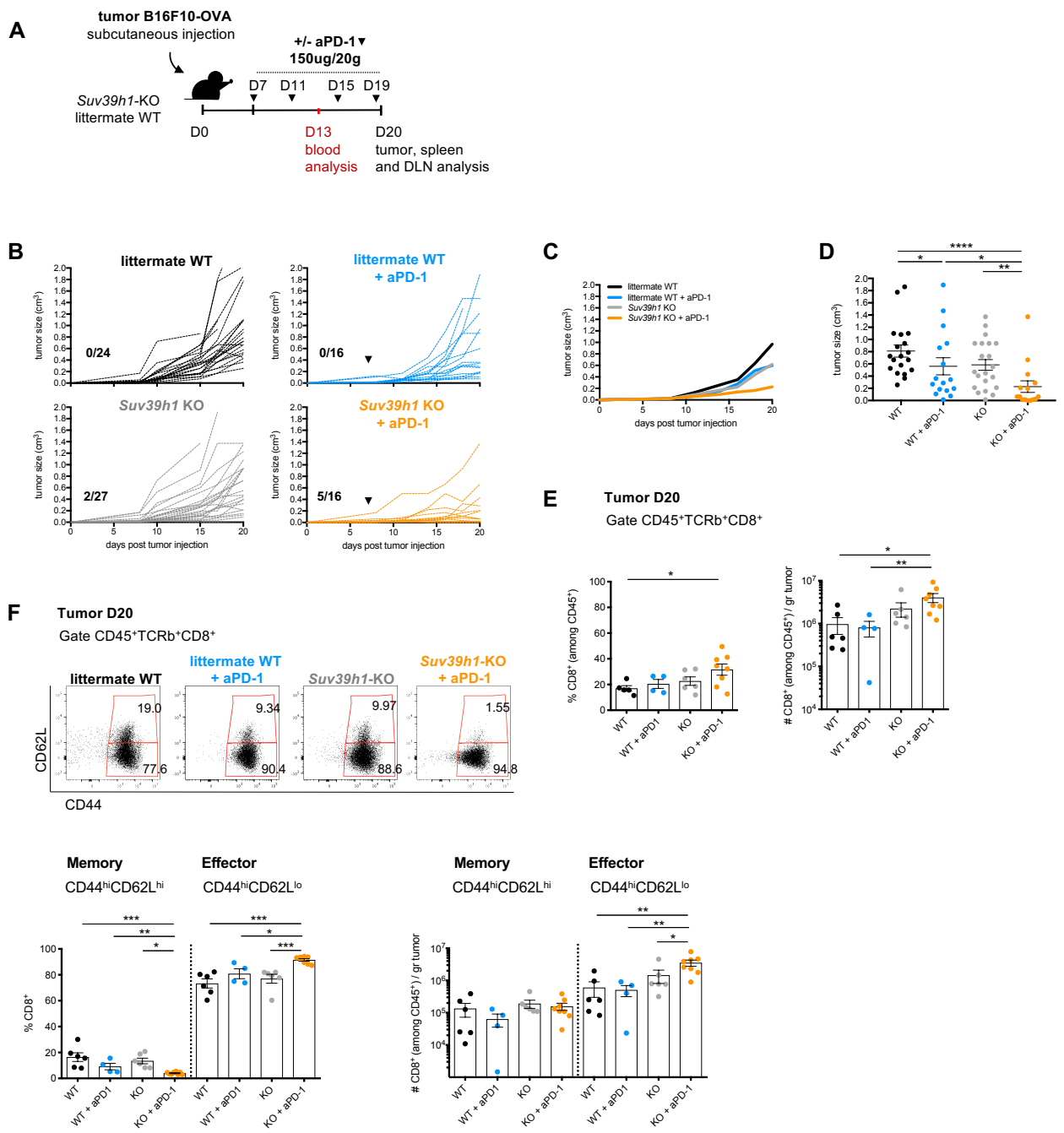


Figure 1. *Suv39h1* deficiency inhibits tumor growth in combination with anti-PD-1 Ab

(A) Graphical representation of model system of experimental groups, including littermates WT and *Suv39h1*-KO mice receiving B16F10-OVA melanoma cells followed by PBS or anti-PD-1 Ab.

(B) Tumor growth kinetics in B16F10-OVA bearing littermate WT and *Suv39h1*-KO mice receiving PBS or anti-PD-1 Ab. Pooled results from three independent experiments are shown. Numbers refer to rejected tumors out of total mice analyzed. Black arrows indicate time point of initial PBS or anti-PD-1 Ab injection.

(C) Tumor growth kinetics. Data is represented as mean.

(D) Tumor volumes in cm³ (at day of sacrifice, day 20).

(E) Frequency (%) and quantification (number) of CD8⁺ TILs (CD45⁺TCRb⁺CD4⁻).

(F) Representative dot plots showing the frequency of memory and effector CD8⁺ TILs from B16F10-OVA tumors, frequency (%) and quantification (number).

p values were calculated using Mann-Whitney test. *p<0.05; **p<0.01; ***p<0.001; ****p<0.0001.

See also Figures S1 and S2.

Fig.2

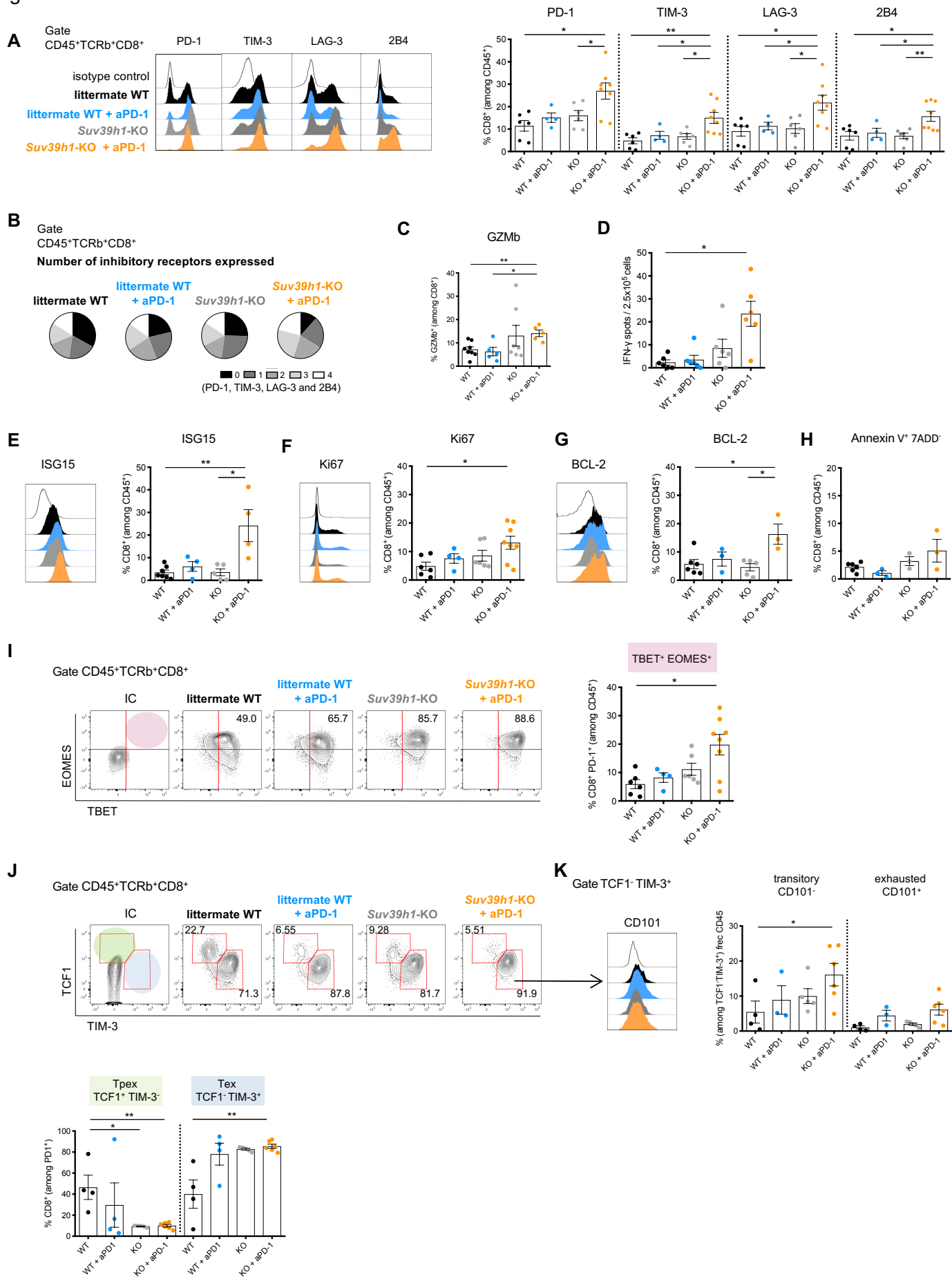


Figure 2. PD-1 blockade in *Suv39h1*-KO CD8⁺ TILs modifies their exhaustion program and enhances their effector capacity

(A) Representative histogram and frequency (%) of inhibitory receptors (PD-1⁺, TIM-3⁺, LAG-3⁺ and 2B4⁺) on CD8⁺ TILs from B16F10-OVA tumors.

(B) Pie chart of co-expression (PD-1⁺, TIM-3⁺, LAG-3⁺ and 2B4⁺) on CD8⁺ TILs from B16F10-OVA tumors.

(C) Representative histogram and frequency (%) of GZMb⁺ cells among CD8⁺ TILs. Cells were re-stimulated in vitro with PMA and ionomycin for 4 hr. (GZMb: Granzyme b).

(D) Blood cells from mice were re-stimulated ex vivo with OVA-I_{SIINFEKL} peptide. The number of OVA-specific T cells producing IFN- γ per 2.5×10^5 blood cells was determined by ELISPOT analysis.

(E) Representative histogram and frequency (%) of ISG15⁺ among CD8⁺ TILs from B16F10-OVA tumors.

(F) Representative histogram and frequency (%) of Ki67⁺ among CD8⁺ TILs from B16F10-OVA tumors.

(G) Representative histogram and frequency (%) of BCL-2⁺ among CD8⁺ TILs from B16F10-OVA tumors.

(H) Frequency (%) of Annexin V⁺ 7ADD⁻ among CD8⁺ TILs from B16F10-OVA tumors.

(I) Representative contour plots and frequency (%) of TBET⁺EOMES⁺ among CD8⁺ PD-1⁺ TILs from B16F10-OVA tumors.

(J) Representative contour plots and frequency (%) of progenitor exhausted (TCF1⁺TIM-3⁻) and late exhausted (TCF1⁻TIM-3⁺) among CD8⁺ PD-1⁺ TILs from B16F10-OVA tumors.

(K) Representative histogram and frequency (%) of transitory (CD101⁻) and exhausted (CD101⁺) among CD8⁺ PD-1⁺ TCF1⁻TIM-3⁺ TILs from B16F10-OVA tumors.

A representative experiment out of two is shown. p values were calculated using Mann-Whitney test. *p<0.05; **p<0.01; ***p<0.001; ****p<0.0001.

See also Figures S3.

Fig.3

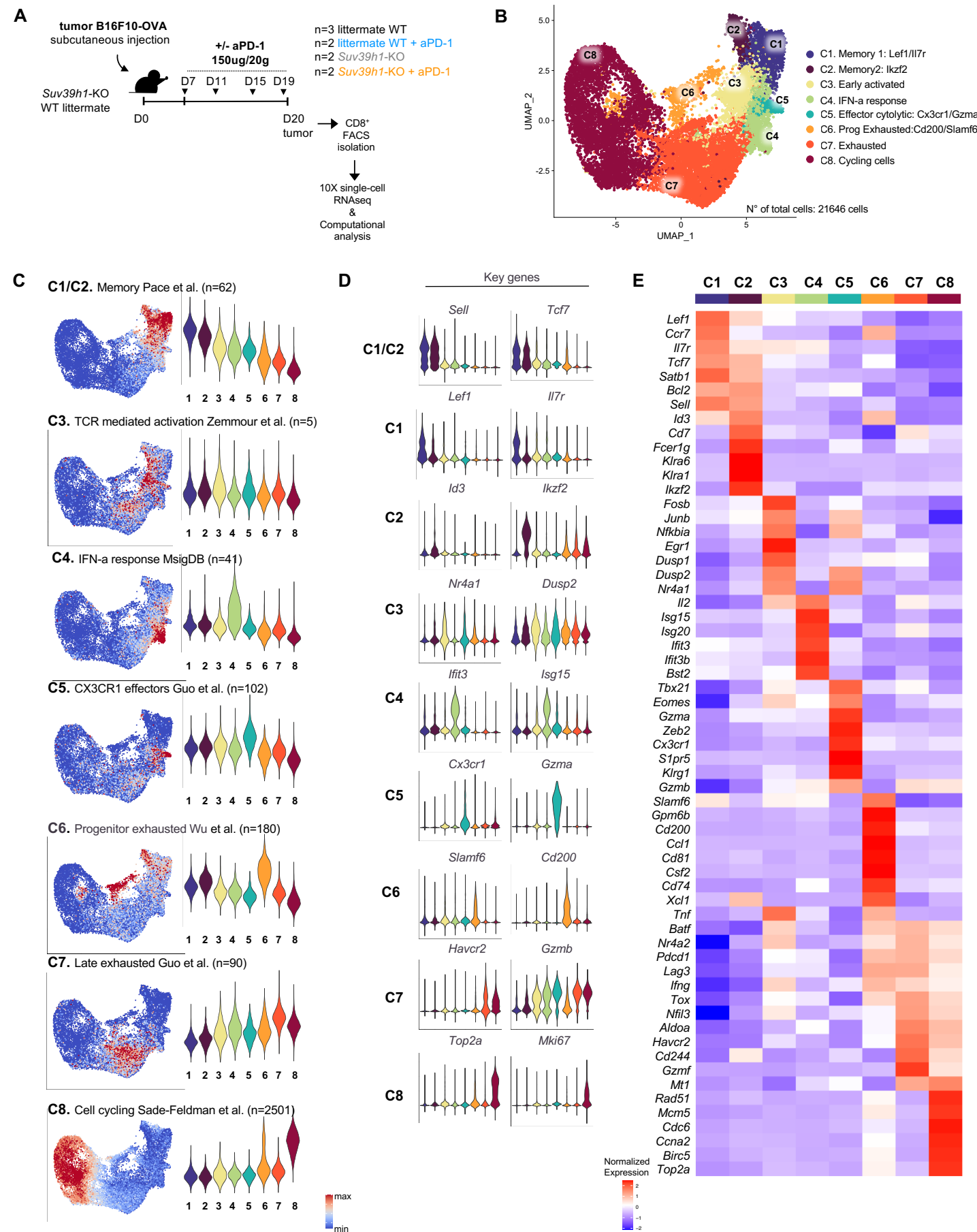


Figure 3. Identification of multiple CD8⁺ TIL populations by single cell RNA sequencing

(A) Scheme of the overall study design. Single-cell RNA sequencing was applied to CD8⁺ TILs isolated from littermate WT and *SUV39h1*-KO mice receiving B16F10-OVA melanoma cells followed by PBS or anti-PD-1 Ab.

(B) UMAP plot with clusters differentiated by colour demonstrating eight distinct CD8⁺ TILs clusters based on gene expression differences for 21646 passing quality control cells. Each dot corresponds to one single cell.

(C) Feature plots and violin plots showing distribution of signature scores indicated by cluster.

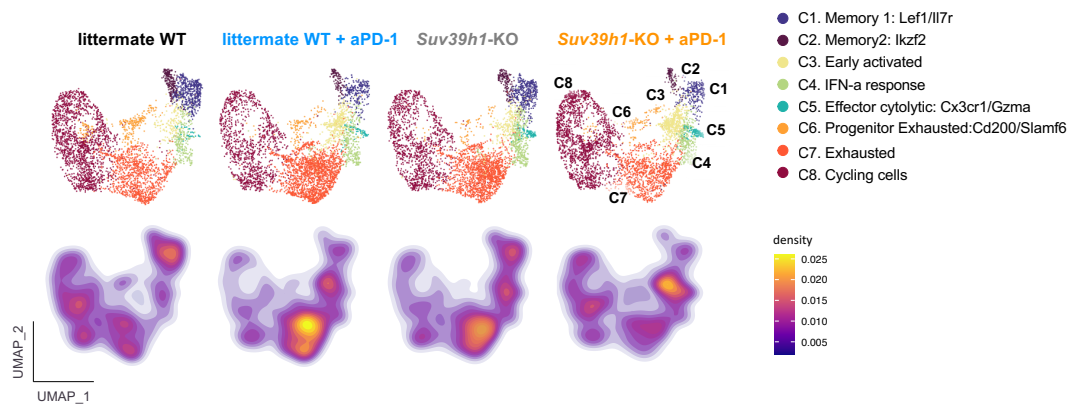
(D) Violin plots showing expression distribution of representative genes for each cluster.

(E) Heatmap showing Z scores for the average expression of selected genes within the eight clusters.

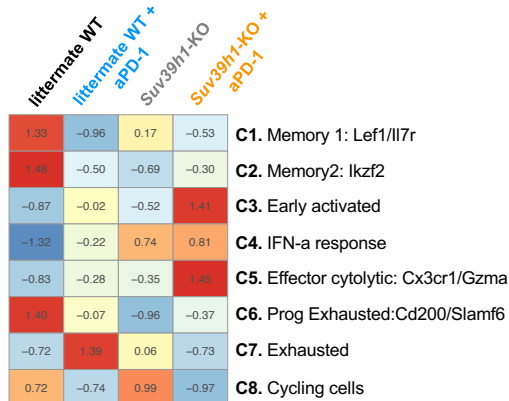
See also Figures S4.

Fig.4

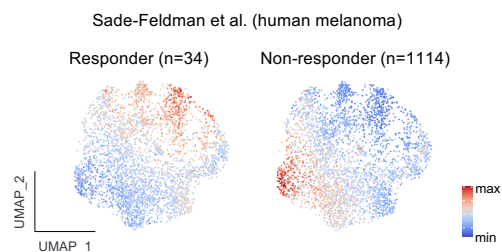
A



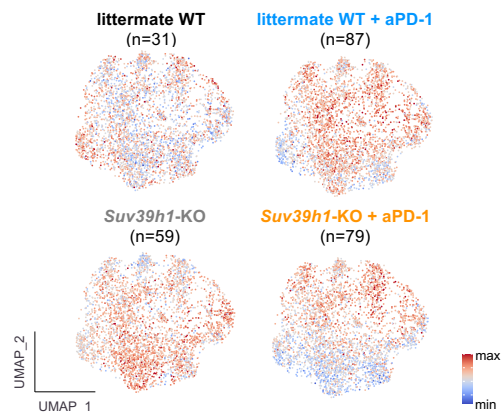
B



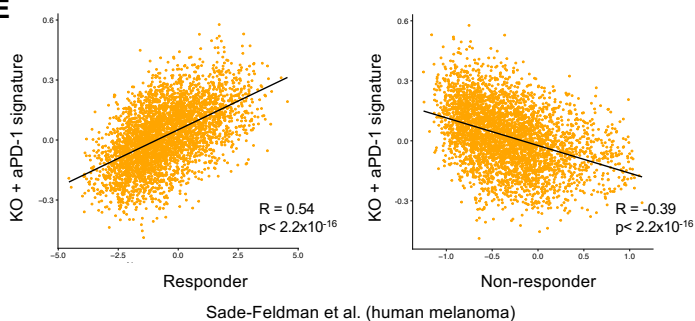
C



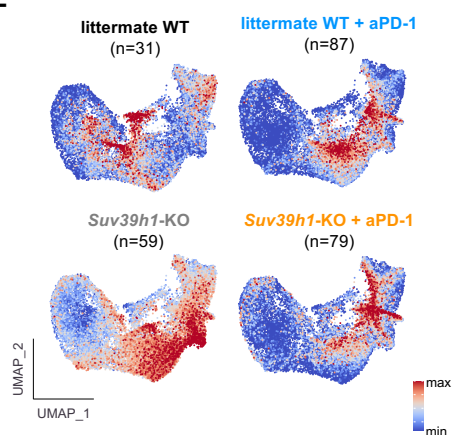
D



E



F



G

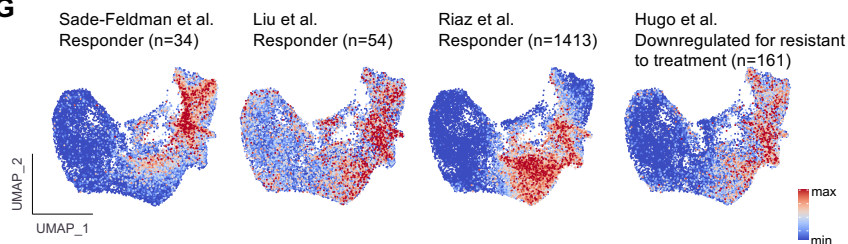


Figure 4. PD-1 blockade in *SUV39h1*-KO CD8⁺ TILs induces a transcriptomic effector phenotype also found in responder melanoma patients

(A) UMAP plot of 4097 cells for each of the four analyzed conditions after downsampling (on the top) and the corresponding density plots (on the bottom).

(B) Heatmap of proportion and numeric value of the downsampled 4097 cells for each of the four conditions within the eight clusters.

(C) Feature plots of human melanoma CD8⁺ TILs showing responder and not responder signature score from scRNAseq published dataset (Sade-Feldman et al., 2018).

(D) Feature plots of human melanoma CD8⁺ TILs showing distribution of signature scores from littermate WT and *Suv39h1*-KO treated or not with anti-PD-1 dataset conditions.

(E) Correlation between transcriptomic signatures from *Suv39h1*-KO mice treated with anti-PD-1 and the responder and not responder melanoma patients (Sade-Feldman et al., 2018) calculated with Person correlation coefficient.

(F) Feature plots of murine CD8⁺ TILs (Figure 3B) highlighting distribution of signature scores of littermate WT and *Suv39h1*-KO treated or not with anti-PD-1 dataset conditions.

(G) Enrichment of the transcriptomic signature of genes upregulated in published melanoma ICB responders projected in murine CD8⁺ TILs UMAP (Figure 3B).

See also Figures S5.

Fig.5

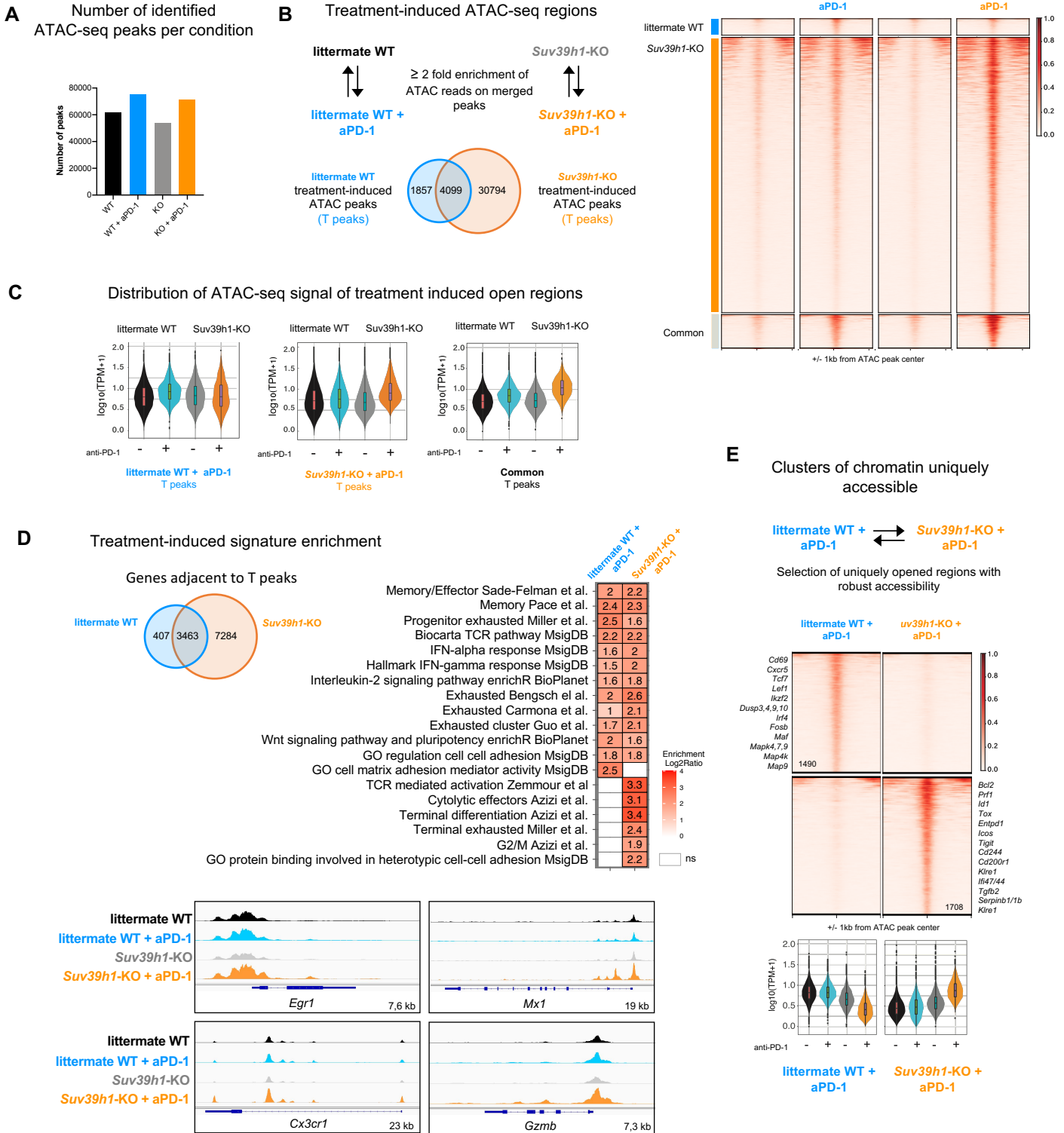


Figure 5. *Suv39h1*-deficiency enhances anti-PD-1 induced chromatin opening at TCR-, cytolytic-, and IFN α - responsive sites

(A) Number of chromatin accessible regions in CD8⁺ TILs of littermate WT and *Suv39h1*-KO mice treated or not with anti-PD-1.

(B) ATAC-seq regions in littermate WT and *Suv39h1*-KO modulated by anti-PD-1 treatment. Venn diagram showing anti-PD-1 treatment modulated peaks in littermate WT, *Suv39h1*-KO, or both (overlap) (middle). Chromatin accessibility heat map grouped by modulated peaks by anti-PD-1 treatment in CD8⁺ TILs of littermate WT, *Suv39h1*-KO, or both (bottom).

(C) Distribution of anti-PD-1 induced ATAC-seq signals in CD8⁺ TILs littermate WT and *Suv39h1*-KO CD8⁺ TILs.

(D) Venn diagram showing number of genes adjacent to anti-PD-1 induced ATAC-seq peaks in littermate WT and *Suv39h1*-KO CD8⁺ TILs (top). Selected signatures enriched in anti-PD-1 induced adjacent peaks open in littermate WT and *Suv39h1*-KO CD8⁺ TILs determined through hypergeometric test alternative greater (middle). Representative ATAC-seq tracks showing accessibility peaks across the loci of *Egr1*, *Mx1*, *Cx3cr1* and *Gzmb* for littermate WT and *Suv39h1*-KO treated or not with anti-PD-1 CD8⁺ TILs (bottom).

(E) Chromatin accessibility heat map grouped by unique differentially accessibility regions in CD8⁺ TILs of littermate WT + anti-PD-1 and *Suv39h1*-KO + anti-PD-1 (top). Distribution of unique anti-PD-1 signals in CD8⁺ TILs of littermate WT + anti-PD-1 and *Suv39h1*-KO + anti-PD-1.

All ATAC-seq data are representative of two biologically independent pooled samples.

Fig.6

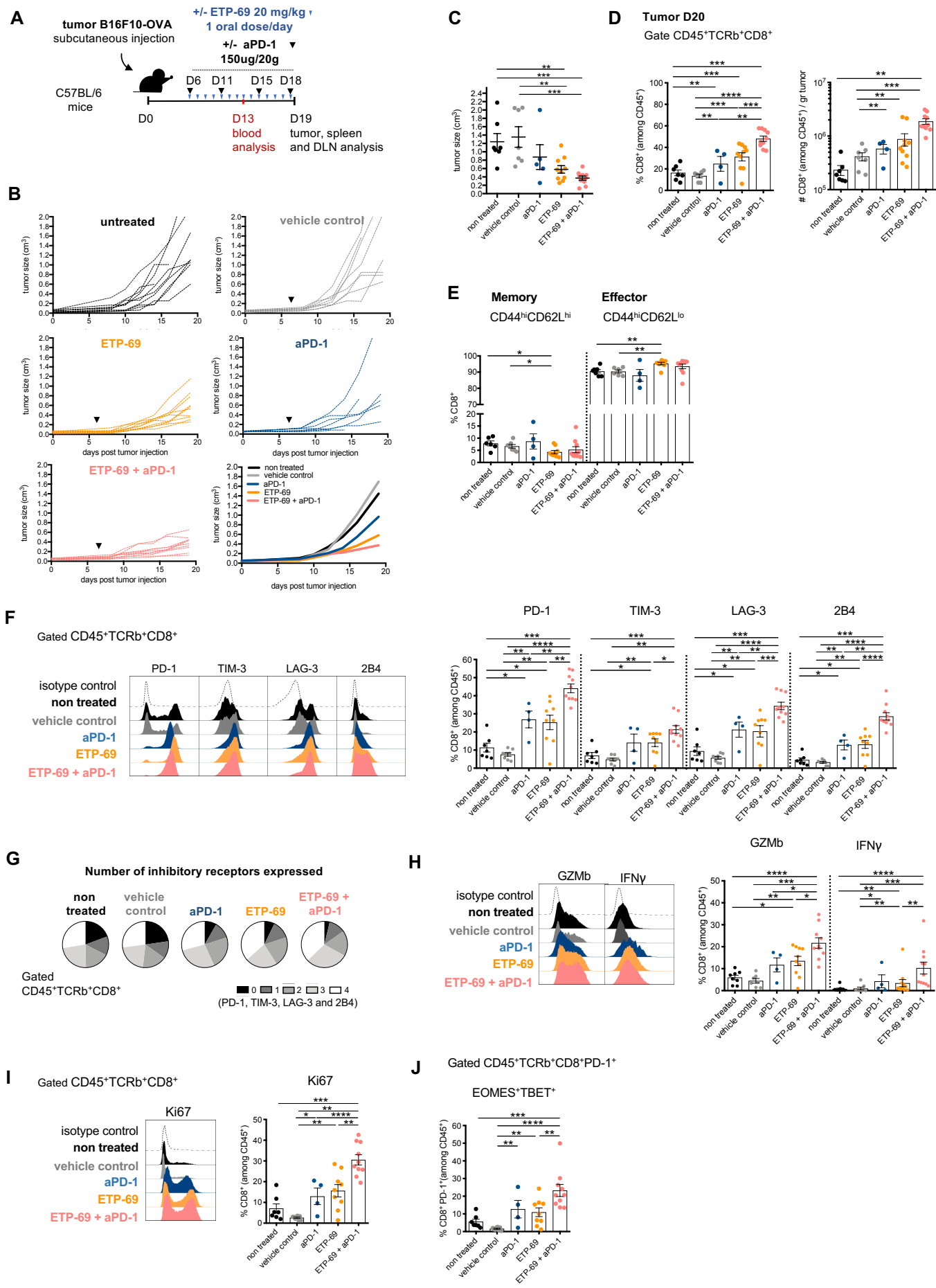


Figure 6. Pharmacological inhibition of Suv39h1 potentiates tumor rejection by anti-PD-1 Ab

(A) Graphical representation of model system of experimental groups, including C57BL/6 mice receiving B16F10-OVA melanoma cells followed by ETP-69 oral treatment, PBS or anti-PD-1 Ab injection.

(B) Tumor growth kinetics represented as means of one representative experiment out of 2; with n=X o X mice per group. Black arrows indicate time of initial ETP-69 or vehicle control dose administration and anti-PD-1 Ab injection.

(C) Tumor volumes in cm³ (on the day of sacrifice, day 19).

(D) Frequency (%) and quantification (number) of CD8⁺ TILs (CD45⁺TCRb⁺CD4⁻).

(E) Frequency (%) of memory and effector CD8⁺ TILs from B16F10-OVA tumors.

(F) Representative histogram and frequency (%) of inhibitory receptors (PD-1⁺, TIM-3⁺, LAG-3⁺ and 2B4⁺) on CD8⁺ TILs from B16F10-OVA tumors.

(G) Pie chart of co-expression (PD-1⁺, TIM-3⁺, LAG-3⁺ and 2B44⁺) on CD8⁺ TILs from B16F10-OVA tumors.

(H) Representative histogram and frequency (%) of GZMb⁺ and IFNγ⁺ cells among CD8⁺ TILs. Cells were re-stimulated in vitro with PMA and ionomycin for 4 hr.

(I) Representative histogram and frequency (%) of Ki67⁺ among CD8⁺ TILs from B16F10-OVA tumors.

(J) Frequency (%) of TBET⁺EOMES⁺ among CD8⁺ PD-1⁺ TILs from B16F10-OVA tumors.

A representative experiment out of two is shown. p values were calculated using Mann-Whitney test. *p<0.05; **p<0.01; ***p<0.001; ****p<0.0001. See also Figure S8.

See also Figures S6.

Fig.S1

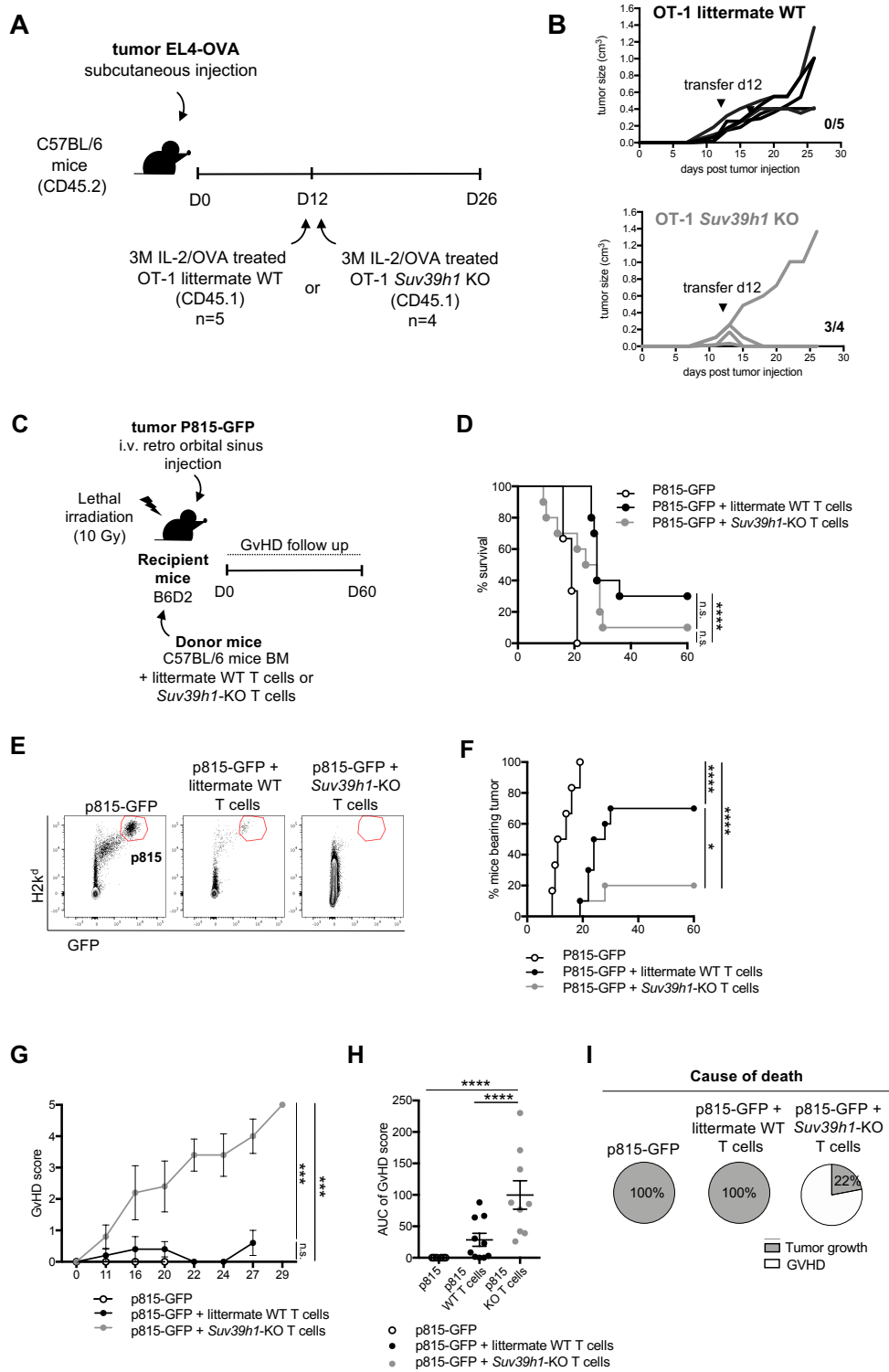


Figure S1. *Suv39h1*-KO CD8⁺ T cells show higher anti-tumoral effects than WT CD8⁺ T cells. Related to Figure 1.

(A) EL4-OVA tumor model. Experimental design. Littermate WT or *Suv39h1*-KO OT-I cells (CD45.1⁺) were activated with IL-2 and OVA-I peptide for 6 days and adoptively transferred (i.v.) to congenic CD45.2⁺ recipient mice bearing EL4-OVA tumor.

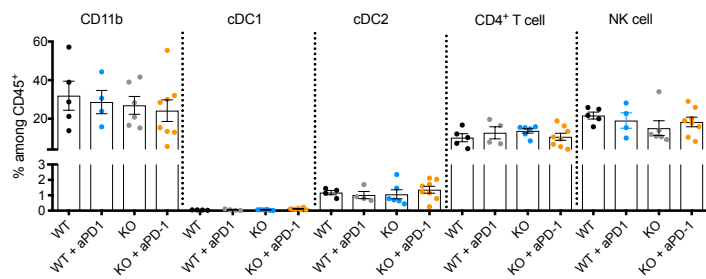
(B) Tumor growth kinetics. Numbers refer to rejected tumors out of total mice analyzed.

(C) P815-GFP tumor model. P815-GFP cells were injected into irradiated B6D2F1 recipient mice grafted with bone marrow cells (n=6), supplemented with littermate WT (n=10) or *Suv39h1*-KO (n=10) CD3⁺ T cells. The experiment was performed twice and the resulting survival (D), tumoral incidence (E-F) and clinical score (G-H) data were pooled. The pie chart (I) represent the proportion of mice dead of leukemia (grey) or GvHD (white). Kaplan-Meier survival curves were compared using log-rank test. For analysis of GvHD clinical grading curves, AUC was calculated for each mouse, and then Student t test or 1-way ANOVA with post hoc analysis was performed depending on number of comparatives. ns, nonsignificant. * p<0.05; **** p<0.0001. **** p<0.0001

Fig.S2 (related Fig.1)

A

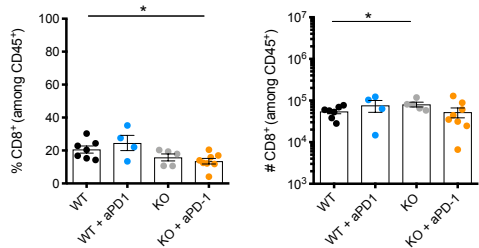
Tumor D20



B

DLN D20

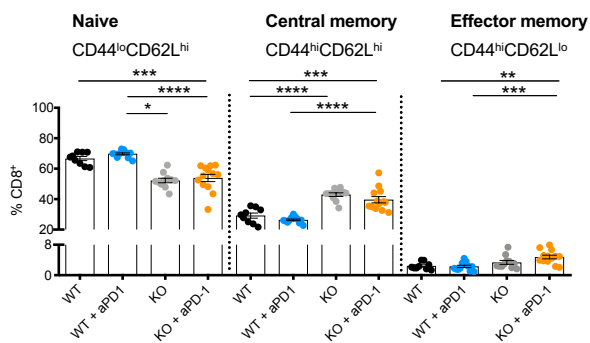
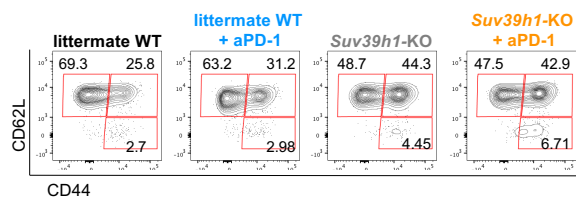
Gate CD45⁺TCRb⁺CD8⁺



C

Blood D12

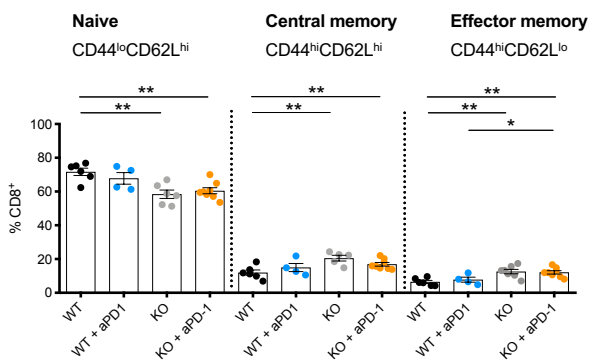
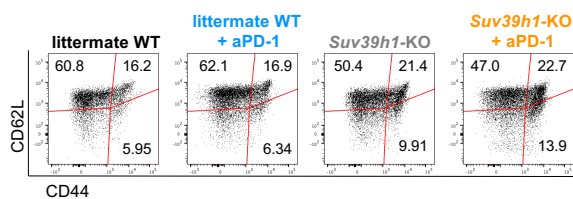
Gate CD45⁺TCRb⁺CD8⁺



D

Spleen D20

Gate CD45⁺TCRb⁺CD8⁺



E

DLN D20

Gate CD45⁺TCRb⁺CD8⁺

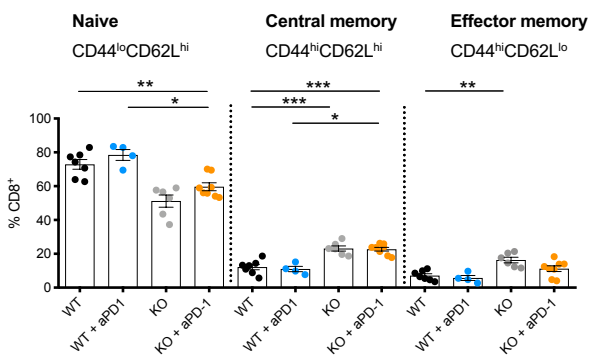
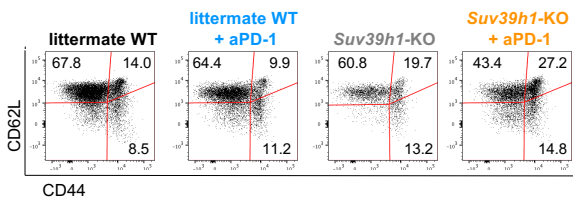


Figure S2. *Suv39h1* is critical for peripheral CD8⁺ T cell differentiation to a memory like phenotype. Related to Figure 2.

(A) Frequency (%) of CD11b⁺, cDC1 (CD45⁺CD64⁺F4/80⁺Lin⁻(CD19⁻, NKp46⁻, TCRb⁻)MHCII⁺CD11C⁺CD26⁺XCR1⁺CD127a⁻), cDC2 (CD45⁺CD64⁺F4/80⁺Lin⁻(CD19⁻, NKp46⁻, TCRb⁻)MHCII⁺CD11C⁺CD26⁺XCR1⁻CD127a⁺) and NK cells (CD45⁺TCRb⁻NK1.1⁺), in B16F10-OVA tumors at day 20 after tumor inoculation.

(B) Frequency (%) and quantification (number) of CD8⁺ in DLN at day 20 after tumor inoculation (CD45⁺TCRb⁺CD4⁻).

(C) Representative contour plots and frequency (%) of CD8⁺ naive, central memory and effector T cells in blood from tumor bearing mice at day 12 after tumor inoculation.

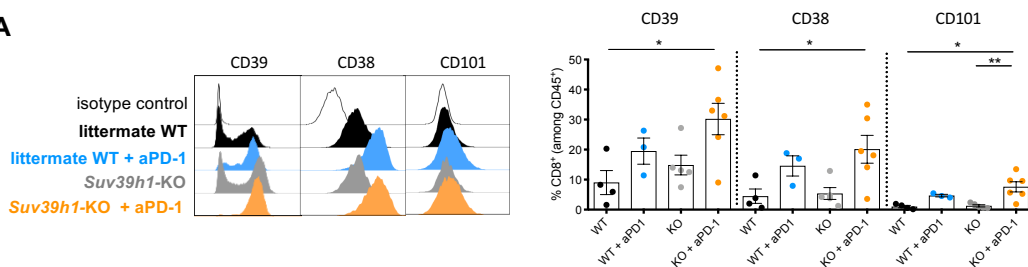
(D) Representative dot plots and frequency (%) of CD8⁺ naive, central memory and effector T cells in spleen from tumor bearing mice at day 20 after tumor inoculation.

(E) Representative dot plots and frequency (%) of CD8⁺ naive, central memory and effector T cells in DLN from tumor bearing mice at day 20 after tumor inoculation.

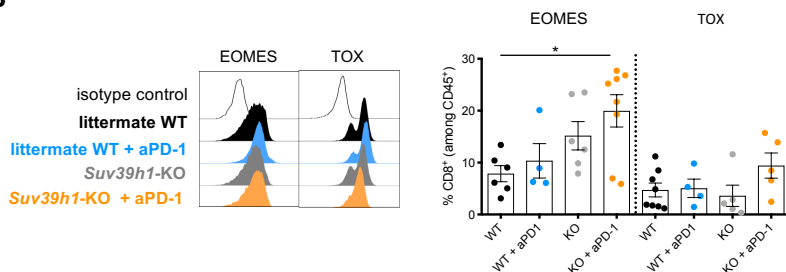
p values were calculated using Mann-Whitney test. *p<0.05; **p<0.01; ***p<0.001; ****p<0.0001.

Tumor D20

A



B



C

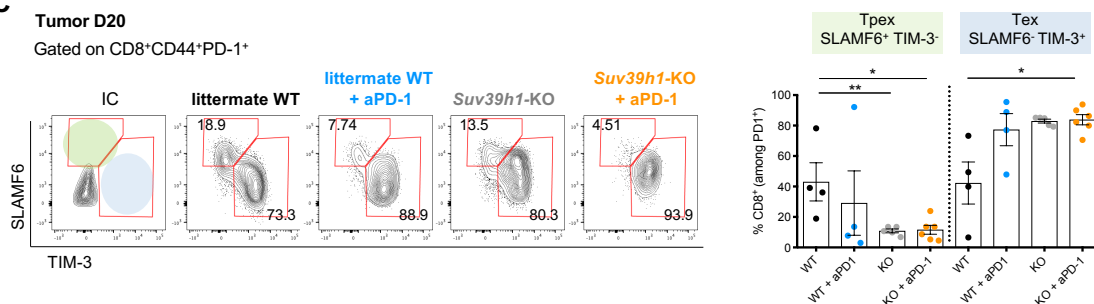


Figure S3. *Suv39h1*-KO mice treated with anti-PD-1 show CD8⁺ TILs with altered effector and exhaustion phenotypes. Related to Figure 2.

(A) Representative histogram and frequency (%) of surface receptors (CD39⁺, CD38⁺ and CD101⁺) on CD8⁺ TILs from B16F10-OVA tumors.

(B) Representative histogram and frequency (%) of transcription factors EOMES and TOX on CD8⁺ TILs from B16F10-OVA tumors.

(C) Representative contour plots and frequency (%) of progenitor exhausted (SLAMF6⁺TIM-3⁻) and late exhausted (SLAMF6⁻TIM-3⁺) among CD8⁺ PD-1⁺ TILs from B16F10-OVA tumors.

Fig.S4 (related Fig.3 and Fig.4)

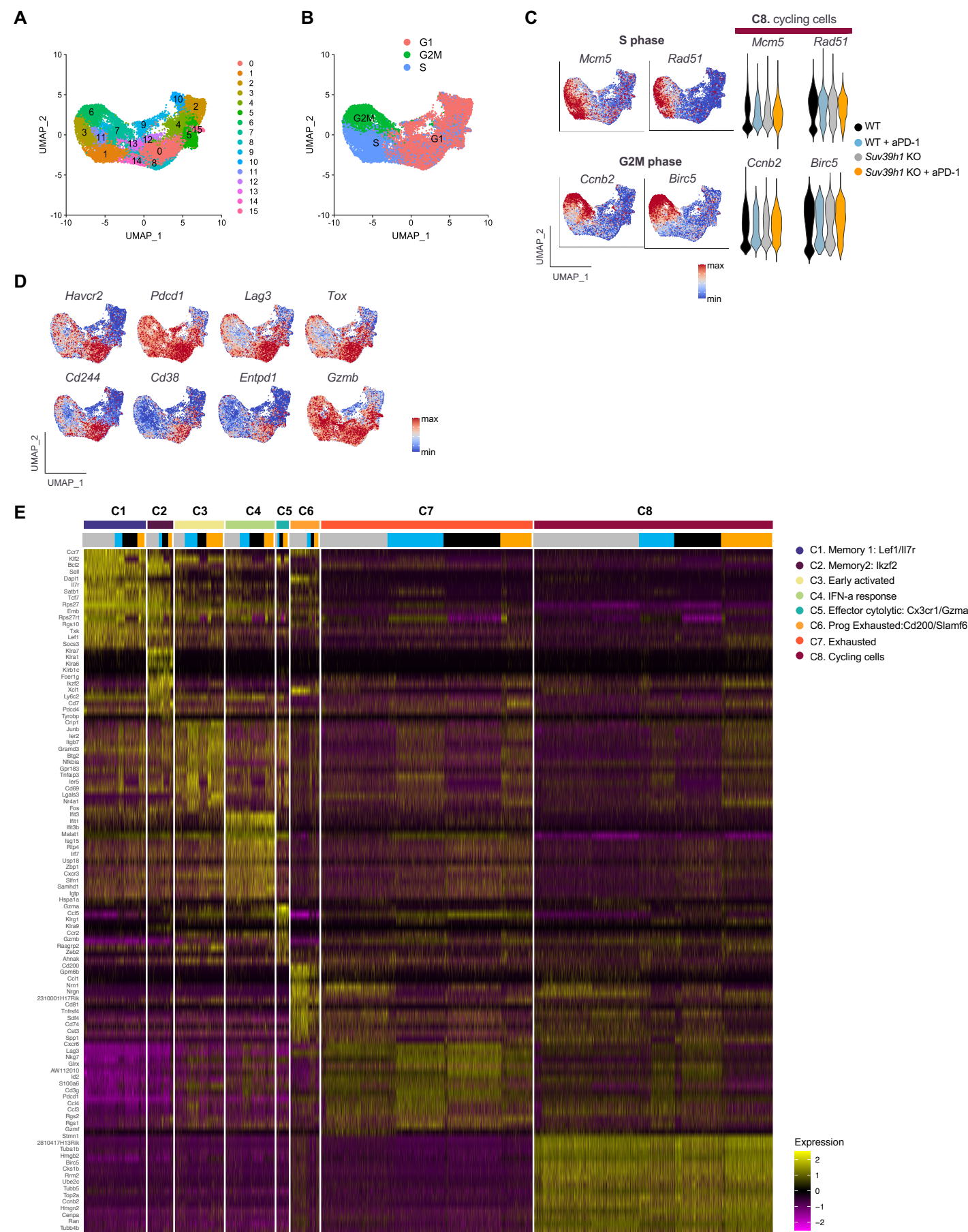


Figure S4. Characterization of CD8⁺ TILs clusters by scRNAseq. Related to Figure 3 and Figure 4.

(A) UMAP plot displaying 16 clusters based on gene expression differences for 21646 passing quality control cells (resolution 0.7). Clusters with matched identities and equivalent CD8⁺ TILs proportions among littermate WT and *Suv39h1*-KO treated or not with anti-PD-1 were merged resulting in a final of 8 clusters (see Fig.3B).

(B) UMAP plot showing cell cycle phases.

(C) Feature and violin plots showing expression of cell cycle phase genes.

(D) Feature plots showing expression of indicated genes.

(E) Heatmap from single-cell analysis of 21646 cells from littermate WT and *Suv39h1*-KO treated or not with anti-PD-1 grouped into clusters. The top 15 genes differentially expressed for each cluster are shown in y axis. Heatmap colour scheme is based on Z-score distribution.

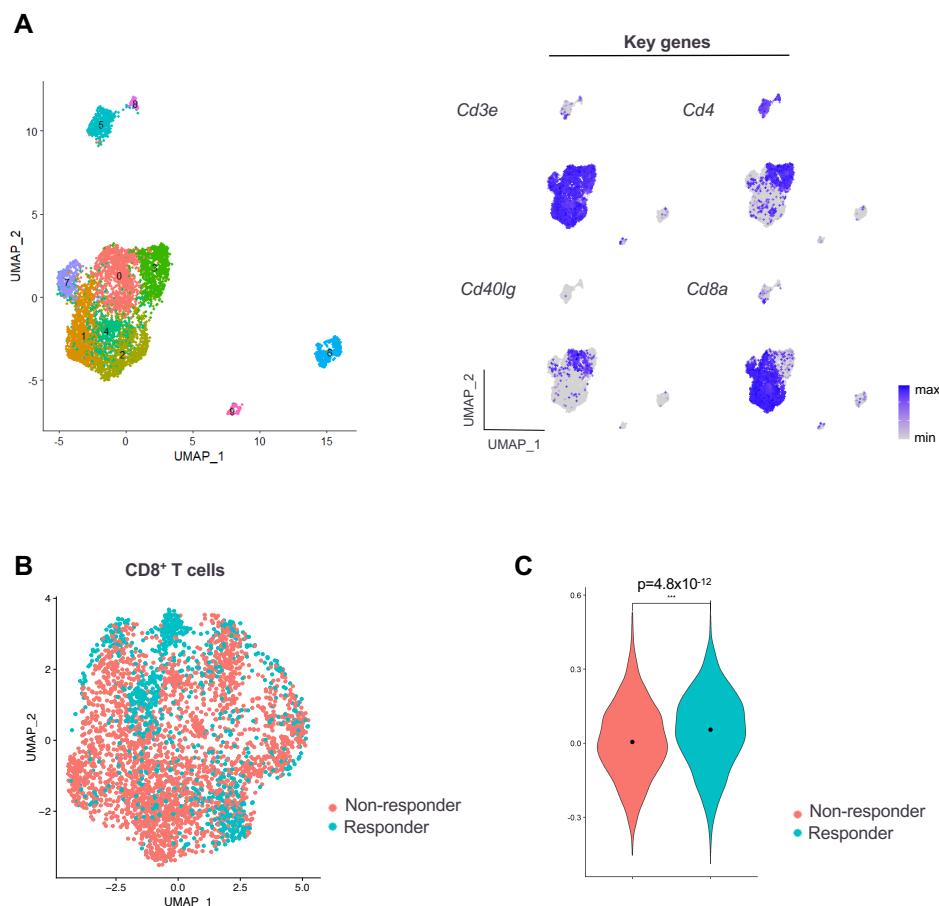


Figure S5. Transcriptomic correlation between human and *Suv39h1*-KO mice responses to immune checkpoint blockade. Related to Figure 4.

(A) To more faithfully compare the human and mice signature of CD8⁺ TILs we first reprocessed the human CD45⁺ single cell data extracted from Sade-Feldman et al. 2018, to generate a new dataset containing only CD8⁺ T cells. Left: UMAP plot displaying scRNAseq of all CD45⁺ from melanoma patient responders and non responders to ICB treatment, before eliminating non CD8⁺ T cells. Right: feature plots showing expression of indicated genes used to conserve CD8⁺ T cells.

(B) UMAP plot displaying CD8⁺ T cells from melanoma patients and identifying CD8⁺ T cells from patients responding or not to ICB treatment (Sade-Feldman et al., 2018).

(C) Violin plots showing the enrichment of signature of genes upregulated in *Suv39h1*-KO + aPD-1 signature projected in CD8⁺ T cells from melanoma patient responders and non responders to ICB treatment (Sade-Feldman et al., 2018).

Fig.S6 (related to Fig.6)

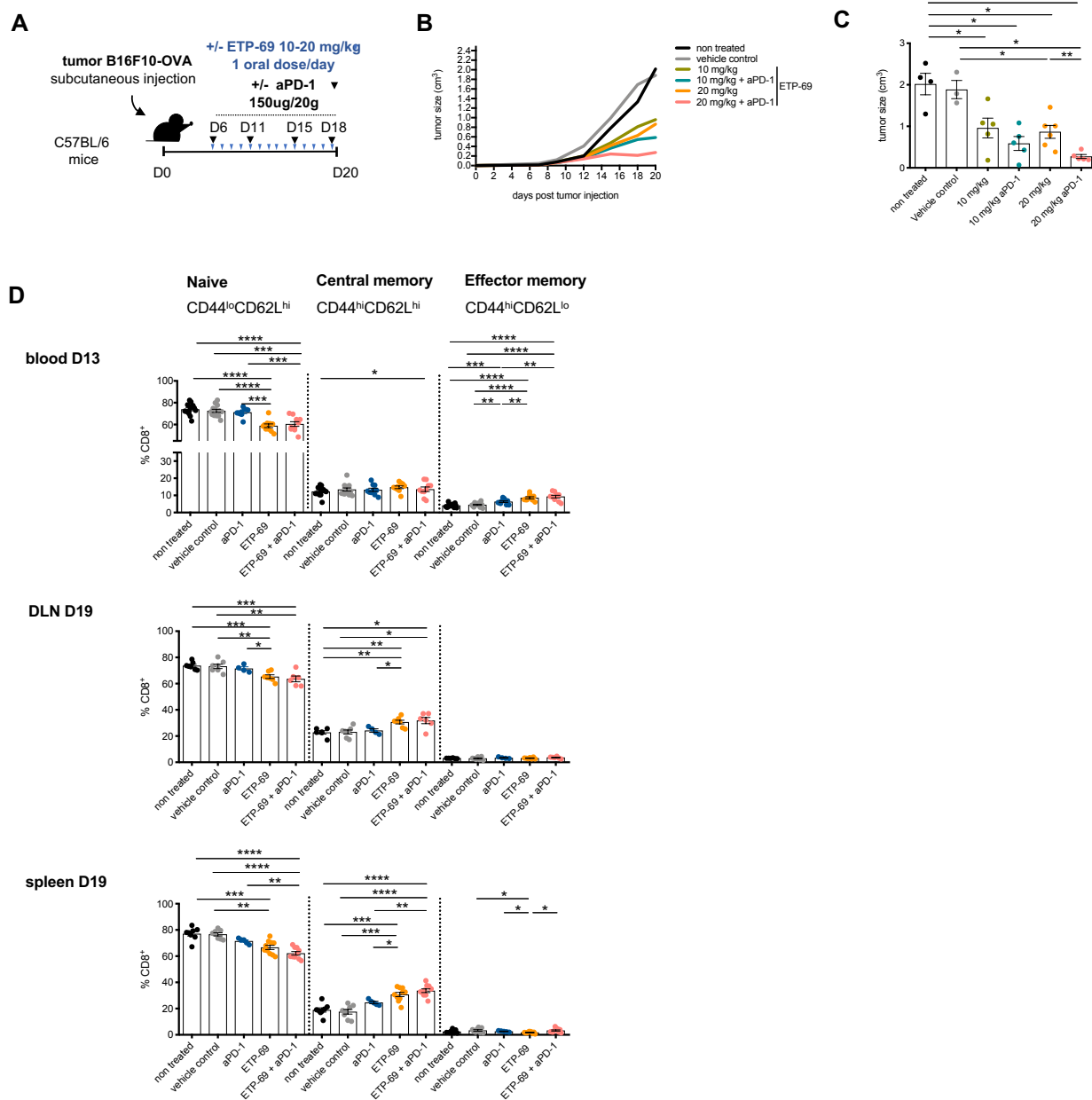


Figure S6. Dose effect of Suv39h1 inhibition combined with immunotherapy. Related to Figure 6.

(A) Graphical representation of model system of experimental groups, including C57BL/6 mice receiving B16F10-OVA melanoma cells followed by ETP-69 oral treatment (10 mg/kg or 20 mg/kg), PBS or anti-PD-1 Ab injection.

(B) Tumor growth kinetics represented as mean of one independent experiment.

(C) Tumor volumes in cm³ (on the day of sacrifice, day 20).

(D) Frequency (%) of CD8⁺ naive, central memory and effector T cells in blood, DLN and spleen from tumor bearing mice at day 12 or day 20 after tumor inoculation.

A representative experiment out of two is shown. p values were calculated using Mann-Whitney test. *p<0.05; **p<0.01.